COMPUTATIONAL ANALYSIS OF FLUID FLOW IN PEBBLE BED MODULAR REACTOR

A Thesis

by

AKSHAY GANDHIR

Submitted to the Office of Graduate Studies of
Texas A&M University
in partial fulfillment of the requirements for the degree of

MASTER OF SCIENCE

August 2011

Major Subject: Mechanical Engineering

COMPUTATIONAL ANALYSIS OF FLUID FLOW IN PEBBLE BED MODULAR REACTOR

A Thesis

by

AKSHAY GANDHIR

Submitted to the Office of Graduate Studies of
Texas A&M University
in partial fulfillment of the requirements for the degree of

MASTER OF SCIENCE

Approved by:

Chair of Committee,	Yassin Hassan
Committee Members,	Tim Jacobs
	Karen Vierow
Head of Department,	Dennis O'Neal

August 2011

Major Subject: Mechanical Engineering

ABSTRACT

Computational Analysis of Fluid Flow
in Pebble Bed Modular Reactor. (August 2011)
Akshay Gandhir, B.S., Texas A&M University
Chair of Advisory Committee: Dr. Yassin Hassan

High Temperature Gas-cooled Reactor (HTGR) is a Generation IV reactor under consideration by Department of Energy and in the nuclear industry. There are two categories of HTGRs, namely, Pebble Bed Modular Reactor (PBMR) and Prismatic reactor. Pebble Bed Modular Reactor is a HTGR with enriched uranium dioxide fuel inside graphite shells (moderator). The uranium fuel in PBMR is enclosed in spherical shells that are approximately the size of a tennis ball, referred to as "fuel spheres". The reactor core consists of approximately 360,000 fuel pebbles distributed randomly. From a reactor design perspective it is important to be able to understand the fluid flow properties inside the reactor. However, for the case of PBMR the sphere packing inside the core is random. Unknown flow characteristics defined the objective of this study, to understand the flow properties in spherically packed geometries and the effect of turbulence models in the numerical solution.

In attempt to do so, a steady state computational study was done to obtain the pressure drop estimation in different packed bed geometries, and describe the fluid flow characteristics for such complex structures. Two out of the three Bravais lattices were analyzed, namely, simple cubic (symmetric) and body centered cubic (staggered). STARCCM+ commercial CFD software from CD- ADAPCO was used to simulate the flow. To account for turbulence effects several turbulence models such as standard k-epsilon, realizable k-epsilon, and Reynolds stress transport model were used. Various cases were analyzed with Modified Reynolds number ranging from

10,000 to 50,000. For the simple cubic geometry the realizable k-epsilon model was used and it produced results that were in good agreement with existing experimental data. All the turbulence models were used for the body centered cubic geometry. Each model produced different results what were quite different from the existing data. All the turbulence models were analyzed, errors and drawbacks with each model were discussed. Finally, a resolution was suggested in regards to use of turbulence model for problems like the ones studied in this particular work.

ACKNOWLEDGMENTS

I would like to thank my parents for all the support that they have given to me over the years. Also, thank you to Dr. Hassan for the research topic and the opportunity to work under him as a Research Assistant. I would also like to thank Angelo Frisani for his assistance and guidance in the initial stages of this project. I want to acknowledge the nuclear engineering computing cluster and Texas A&M Hydra cluster for providing the computing resources for this study. Finally, I would like to thank my friends for all their insight and support during my graduate work.

TABLE OF CONTENTS

CHAPTER Page

LIST OF TABLES

LIST OF FIGURES

FIGURE Page

CHAPTER I

INTRODUCTION

Majority of fluid flows that exist in our surrounding are inherently turbulent in nature. Understanding such common type of flows is extremely crucial and would result in great benefit and breakthrough in the field of science and technology. Proper understanding of such flows is important because turbulence affects many other existing phenomena and can be used to make many challenging processes easy and efficient. For example, turbulence enhances the heat transfer from a solid to a liquid, turbulence enhances fluid mixing that is useful in many applications such as reacting flows, etc. However, computational and experimental investigations of such flows with proper data validation and verification is extremely difficult. Currently, majority of turbulent flows that we encounter in our society are at a Reynolds number that can not be fully resolved. Nonetheless, experimental and computational efforts to analyze high Reynolds number flows are made in current research activities.

Experimental analysis of only a few types of flows is possible because of experimental cost and feasibility issues. Computational analysis of turbulence is much more feasible and cheap. Therefore, correct or mostly accurate computational analysis of turbulence is important and will be beneficial for great advancement in research and technology. This can be done by computational analysis of various existing turbulence models and comparison with experimental results for similar cases for data validation. This process of data verification along with data validation would help analyze various turbulence models and assist in determining the optimum model that can be used for future design purposes of a particular technology.

The journal model is *IEEE Transactions on Automatic Control.*

Pebble Bed Modular Reactor (PBMR) is one such design that requires fluid flow analysis in the nuclear energy industry. Several research attempts have been made previously to analyze the fluid flow inside the core of pebble bed reactors. The core of PBMR consists of spherical objects that are oriented in a random fashion. Flow around a single sphere is a complex and inherently unsteady phenomenon and many attempts to computationally analyze such flows have been made. [1][2][3] From observation, fluid flow behind a spherical objects results in a wake formation and existence of a flow structure referred to as "Von-Karman" vortex streak has been made from decades. However, a combination of multiple spheres, like in the core of PBMR core, and that too in a random orientation makes modeling the fluid flow extremely difficult and the choice of turbulence model extremely crucial.

It is important to analyze the fluid flow characteristics and expected flow structure in PBMR core for reactor safety and reactor design concerns. Previous, research has shown hot spots being generated by the formation of vortices downstream due to complex flow separation in such geometries. [4] Hot spots can also affect the material integrity of th fuel which again is a critical issue in the nuclear industry. Along with the fluid flow, a pressure drop analysis is crucial as well from a reactor design standpoint. Significant amount of research is being conducted for the PBMR design. Research which includes applying various turbulence models to predict the flow structure inside the PBMR core. One methodology is to use Reynolds Averaged Navier Stokes (RANS) turbulence model to obtain the flow structure inside the core geometry. This poses a question of which RANS model would be better for such a study? Extensive research is being conducted for the PBMR due to its increasing interest in the nuclear industry which is motivated by the view that new nuclear power reactors will be needed to provide low carbon generation of electricity and possibly hydrogen production to support the future growth in demand for both of these commodities.

[5] Identifying a turbulence scheme that would model the flow in such geometries with acceptable errors would be extremely beneficial. It would foremost result in better understanding of the turbulence physics and its effects in the PBMR core, along with improvements in the PBMR core design analysis, also it is extremely important to conduct such a study for flow in the PBMR core from a safety perspective. [6]

The main objectives of this study from the points mentioned above are the need to study the fluid flow in geometries comprised of spheres, the effect of the various turbulence models on the numerical result and expected pressure drop estimation if the PBMR core.

CHAPTER II

HIGH TEMPERATURE GAS COOLED REACTOR

A High Temperature Gas-cooled Reactor (HTGR) is one of the renewed reactor designs to play a role in nuclear power generation.[7] HTGR is the Generation IV reactor concept in the nuclear industry. HTGR technology has two main added benifits when compared with existing nuclear reactors. Firstly, HTGR offers inherent safety features that eliminate the need for active safety systems. Secondly, HTGR would enable hydrogen production with an addition of a thermo chemical cycle in the design and that generated hydrogen can be used as extra fuel. Fig. 1 shows a general schematic of HTGR concept that was introduced by Department of Energy in its Generation IV nuclear reactor concept road map.

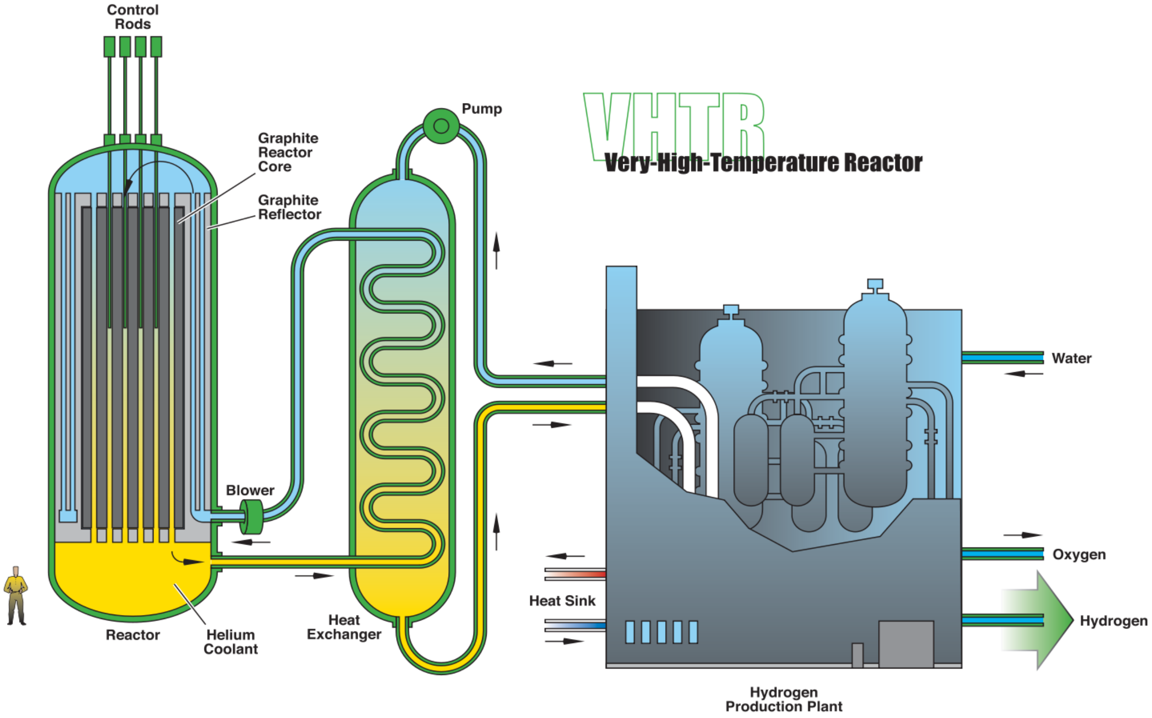

Fig. 1. Department of Energy's High Temperature Gas-Cooled Reactor schematic [8]

The HTGR reactor design, during normal operating conditions, can have reactor coolant outlet temperature to a value of 1000 degrees C or higher with a net thermal efficiency of 50% or higher. However, DOE specified certain key studies that need to be conducted that would demonstrate viability of such reactors. Novel fuels and materials must be developed that: [8]

1. Permit increasing the core-outlet temperatures from 850 degrees C to 1000 degrees C and preferably even higher
2. Permit the maximum fuel temperature reached following accidents to reach 1800 degrees C
3. Permit maximum fuel burnup of 150200 GWD MTHM
4. Avoid power peaking and temperature gradients in the core, as well as hot streaks in the coolant gas.

The HTGR, also reffered to as Very High Temperature Reactor (VHTR), can be divided into two main categories, namely, prismatic block reactor and pebble bed reactor. The difference between the two types being the design of the reactor core, which is a prismatic block for prismatic block reactor and consisting of fuel pebbles for pebble bed reactor. In this study, fluid flow analysis in the reactor core of only pebble bed reactor is conducted and this particular type of reactor is discussed further.

A. Pebble Bed Modular Reactor

PBMR falls under the category of VHTR, it is one the six designs that fall in DOE's Generation IV nuclear initiative.[8] The pebble bed reactor design was first introduced in 1985 by Sefidvash. His initial design was a modular light water reactor fluidized bed. [9] However, Sefidesh's initial design was modified from a light water reactor to a gas cooled reactor. This was done to avoid the complications of multi-phase phenomenon at high operating temperatures. The new PBMR concept is designed to used Helium gas as the operating coolant that will help convert the thermal energy from nuclear reaction in the reactor core into electrical energy. There are two Pebble Bed designs that are being developed in the world. A 10 megawatt prototype reactor in China and a modular pebble bed reactor in South Africa with a rated capacity of 165 MWe. In this report, only the features of PBMR design in South Africa will be discussed.

1. Thermodynamic Design

The PBMR uses a thermodynamic Brayton cycle to convert thermal energy into electrical energy. [7] A schematic of the PBMR design is shown in Fig. 2

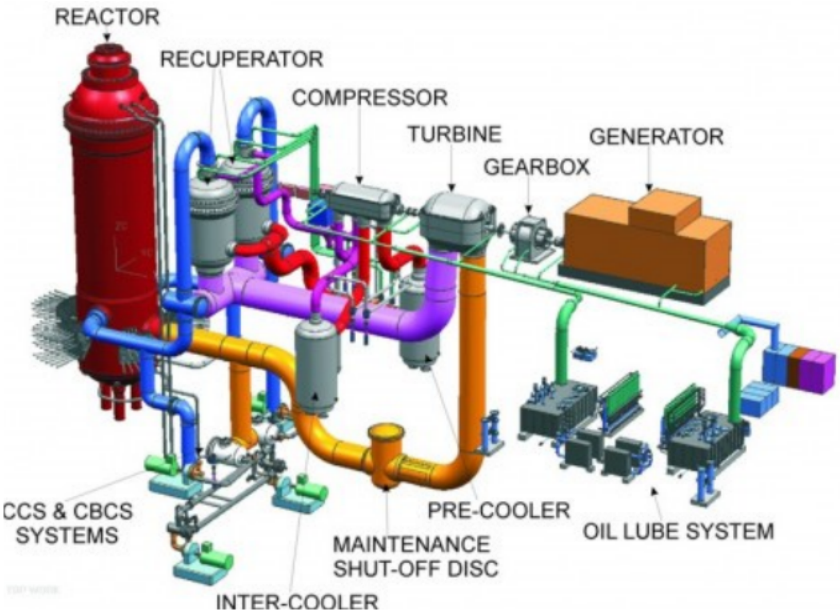

Fig. 2. Pebble Bed Modular Reactor's plant design

The coolant, Helium gas, enters the reactor core from top of the core at an inlet temperature of about 500 degrees C. Inside the reactor core the coolant is heated from the heat produced through the fission reaction of the nuclear fuel inside the reactor core. The Helium gas exits the reactor at an temperature of about 1000 degrees C. During normal operating conditions, the reactor core is maintained at a pressure of 8.5 MPa. Helium at high temperature flows out of the reactor core to the turbine that is used to drive the generator that produces electricity. The Helium gas, after flowing through the turbine enters the recuperator where it loses energy by pre-heating the Helium gas that is about to enter the reactor core through the cold leg. From the recuperators, the Helium gas goes through the inter-cooler and pre-cooler system. Afterwards, the coolant (He gas) gors through the compressor and re-enters the reactor core at the inlet temperature of about 500 degrees C.

Helium as the active coolant as opposed to light water, suggested by Sefidesh in his original design, has many benefits. Some of these are listed below:

1. Helium is an inert gas and thus will not chemically react with other materials in the system. [10]
2. Helium does not become radioactive upon exposure to neutron radiation.[11]
3. Helium has been used for other processes at high temperature and therefore there is plenty of experience and understanding about its behavior at high temperatures.

The pressure vessel, referred to as “REACTOR”, in Fig. 2 is made from steel on the outside. It is about 6 meters in diameter and about 20 meters tall. The steel vessel encloses a graphite shell that surrounds the fuel spheres. The graphite shell has two main benefits, firstly, it acts as a outer reflector for the neutron flux that helps keep the reactor at a critical state. Secondly, it acts as heat sink by acting as a passive heat transfer medium during reactor emergency conditions.

2. PBMR Fuel

The active fuel in the PBMR, in fact in both the VHTR designs, is Uranium dioxide. PBMR fuel is a special type of fuel design that is referred to as TRISO (Tristructural-isotropic) fuel. Fig. 3 shows a schematic of the fuel spheres that are placed inside the reactor core. The fuel spheres are 60 millimeters in diameter (about the size of a tennis ball). The fuel sphere itself is made up of 5 millimeter thick graphite that encapsulates many coated fuel particles.

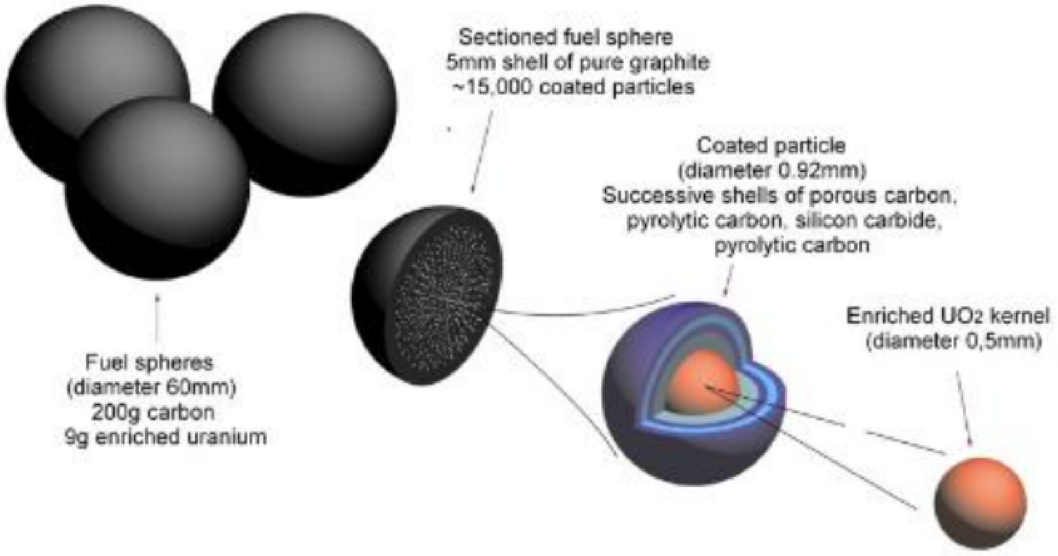

Fig. 3. Pebble Bed Modular Reactor's fuel pellet

Each fuel particle has an outer layer of pyrolytic carbon, which is a dense form or heat-treated carbon. Inside the outer carbon coating there exists a silicon carbide coating that acts as a neutron reflector. Under the silicon carbide coating there is another pyrolytic coating. Under that, there is a Porous carbon buffer that helps contain all the fission products released from the kernel without over-pressurizing the coated particle. Under the carbon buffer layer, in the middle of the fuel particle resides the active fuel in the PBMR, Uranium oxide kernel, which is about 0.5 millimeter in diameter.

Overall the core of PBMR consists of approximately 360,000 spherical fuel pebbles distributed randomly. Each of the fuel spheres inside the reactor core contains about 15,000 fuel particles. About 3,000 pebbles handled by Fuel Handling Service (FHS) each 7 day. About 350 discarded daily. One pebble discharged every 30 seconds. Average pebble cycles through core 15 times. Fuel handling is most maintenance- intensive part of plant. [12]

CHAPTER III

COMPUTATIONAL ANALYSIS APPROACH

For the computational analysis in this study, CD_ADAPCO's StarCCM+ version 3.006 was used. The CAD design of the geometry was developed using a commercial software called Solidworks. Thereafter, the CAD design was transferred to StarCCM+ where the meshing and simulation was run.

A. Designs

One of the objective of this analysis was to analyze the fluid flow inside th PBMR core. As mentioned earlier, the core of PBMR is comprised of fuel spheres that are randomly distributed. Therefore, obtaining the exact geometric description of the reactor core is basically impossible. This posed a big problem as far as the computational analysis of the PBMR core was concerned. However, since this was a design analysis, the main objective became determining the extremes inside the core and common flow features that would be expected in the geometry made of spheres. From fluid mechanics, we know that in a geometry that is comprised of spheres, the flow properties depend on a geometric variable, and that is the geometric porosity. Mathematical representation of porosity is shown in Eq. 3.1, basically, it is a ratio of the void volume to the total volume of the geometry.

$$\eta = Porosity = \frac{V_F}{V_T} \tag{3.1}$$

The flow properties are dependent on this porosity variable, for example, a higher porosity would result in a lower pressure drop or velocity and vica-versa.

This dependence of flow properties on a geometric variable made enabled us to limit the analysis to two types of geometries, one with highest porosity and the other with lowest porosity. At this point, three Bravais lattices were compared, namely, simple cubic, body centered cubic and face centered cubic. Out of the three geometries, only simple cubic and body centered cubic were analyzed. This is because the simple cubic geometry has the highest porosity whereas the body centered cubic geometry has the lowest.

1. Simple Cubic Design

Fig. 4 shows the cubic lattice structure of the simple cubic design. This particular geometry has the highest porosity.

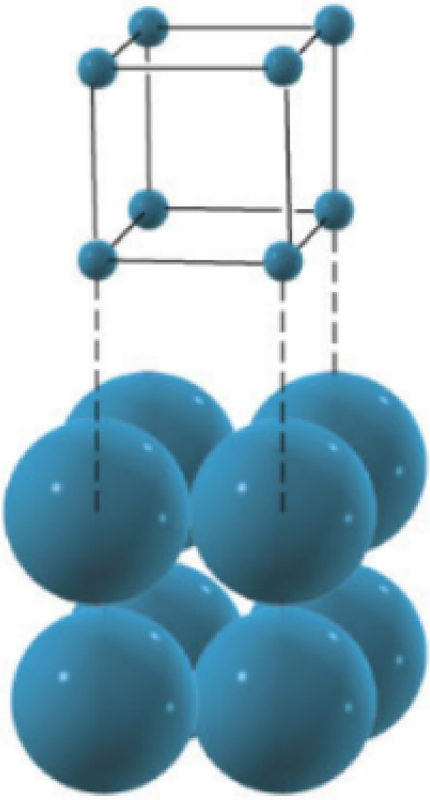

Fig. 4. Cubic lattice of simple cubic design

The computational geometry used for this geometric design was a 5 X 5 X 5 structure as shown in Fig. 5.

Fig. 5 represents the fluid region of a 5 X 5 X 5 design and a geometric design that

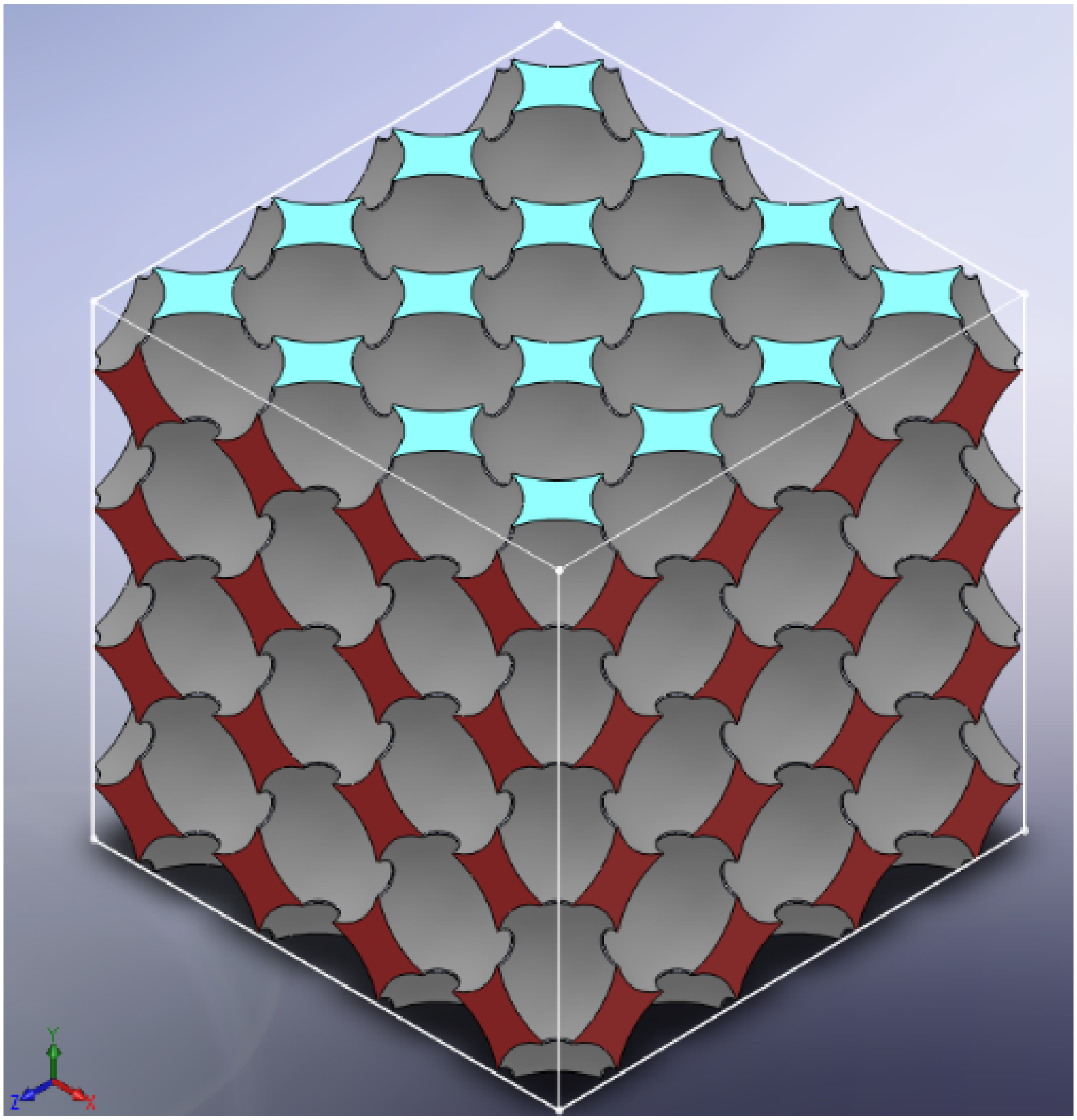

Fig. 5. Computational geometry of simple cubic design

represents the fluid region of the geometry. The computational geometry used for the simple cubic design has a porosity of 0.45. In Fig. 5 the blue plane represents velocity inlet plane, the red plane represents a symmetry plane, which is on all four sides and one the opposite side of the inlet plane is the pressure outlet plane. Geo-

Table I. Simple Cubic Geometry Specifications

Pebble Size	Number of Elements	Corresponding Spheres
Ocatant	8	1
Quater	36	9
Half	54	27
Full	27	27
Total	125	64

metric distribution in this form is used further for meshing and Computational Fluid Dynamics (CFD) analysis.

Table I describes the geometric details of the 5 X 5 X 5 geometry. It contains a total of 64 full spheres that are made up from 125 individual spheres.

2. Body Centered Cubic Design

The body centered cubic geometry has the lowest porosity out of all the three Bravais lattices. Fig. 6 shows the cubic lattice structure for this particular lattice. The computational geometry used for this geometric design was a 2 X 2 X 3 structure as shown in Fig. 7. This particular geometry has a porosity of 0.303.

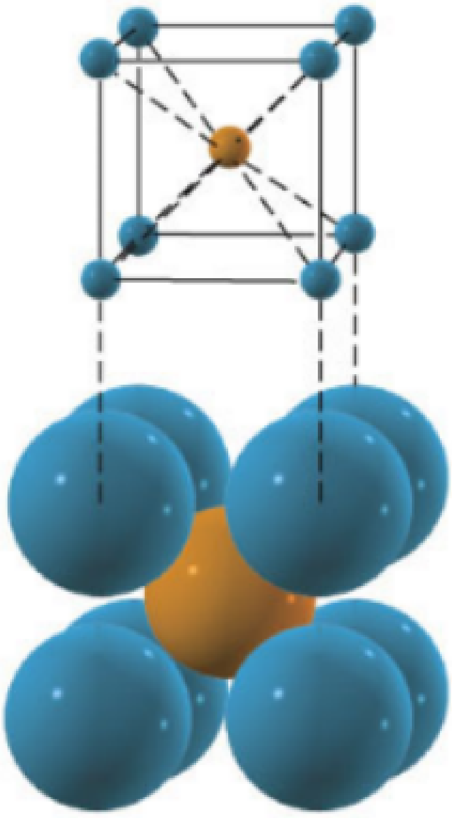

Fig. 6. Cubic lattice of body centered cubic design

Fig. 7 represents the solid region and the fluid region that is used for the CFD analysis is shown in Fig. 8.

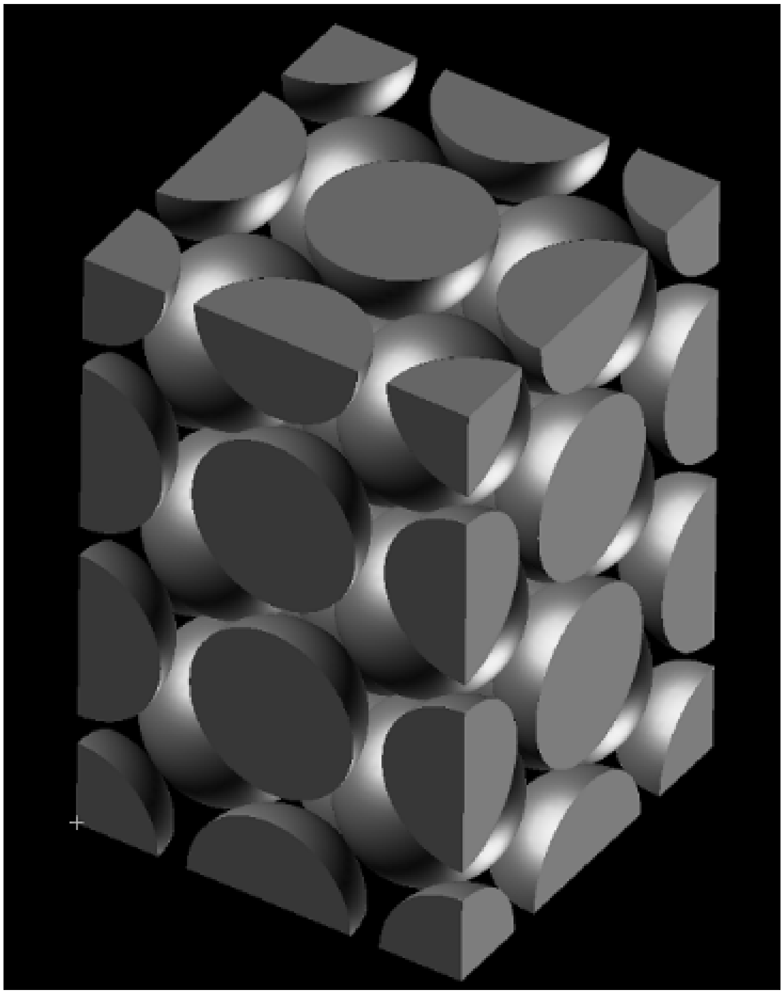

Fig. 7. Computational geometry for body centered cubic case (solid region)

The green faces in Fig. 8 represent the symmetry plane, the top plane represents the velocity inlet plane and the plane opposite to inlet plane (which can not be seen in the image) is pressure outlet plane.

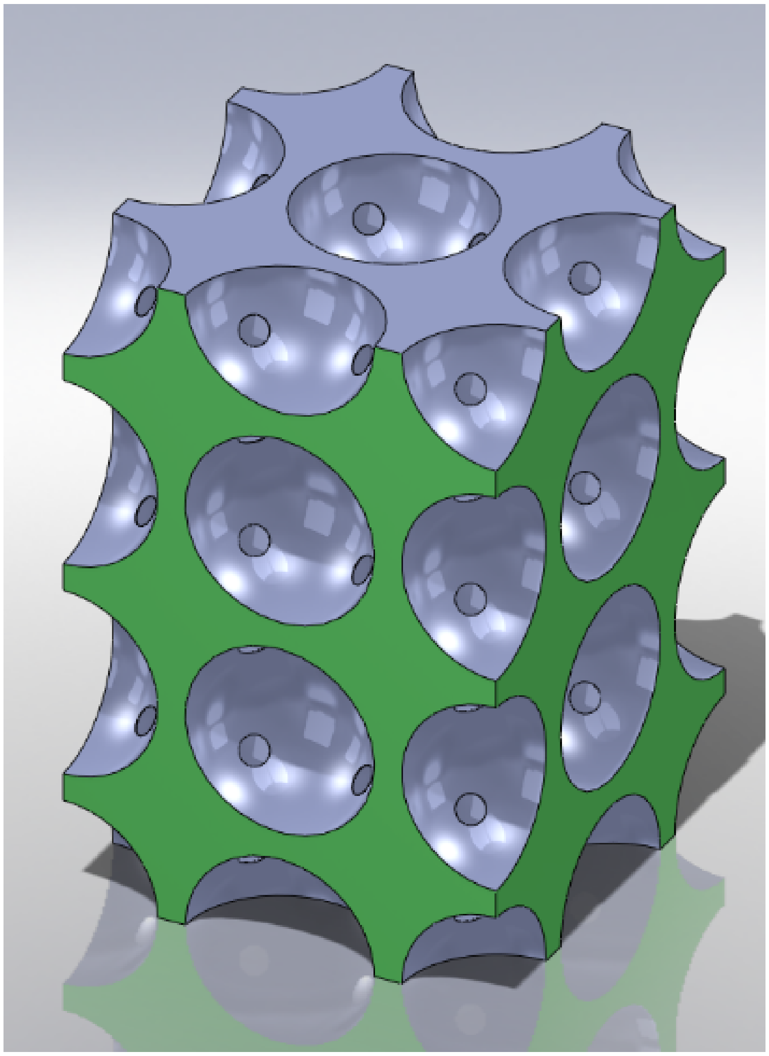

Fig. 8. Computational geometry for body centered cubic case (fluid region)

Table II describes the geometric details of the 2 X 2 X 3 geometry. It contains a total of 24 full spheres that are made up from 48 individual spheres.

Table II. Body Centered Cubic Geometry Specifications

Pebble Size	Number of Elements	Corresponding Spheres
Ocatant	8	1
Quater	16	4
Half	10	5
Full	14	14
Total	48	24

B. Mesh Continuum

For the simple cubic design six different polyhedral meshes were created that ranged from five hundred thousand to ten million. Table III shows the cell information for the six meshes created for the simple cubic design.

Table III. Simple Cubic Meshes

Mesh Number	Number of Prism Layers	Total Number of Cells
1	2	563,283
2	2	737,735
3	2	1,068,483
4	2	2,583,764
5	5	4,536,619
6	2	10,272,720

Mesh creation for both the designs had complications at the sphere contacts. This is because, two spheres connect at a point and dividing a point into discretized area is not possible. To avoid this problem we made the two neighboring spheres intersect and using the cross-sectional area as the plane of contact. This of course adds some error in our calculation. However, our assumption is that this error is relatively small for pressure drop calculation. Fig. 9 shows the sphere contact point and the modification that was implemented to avoid the contact point issue.

For the simple cubic design, the mesh with the 10 million cells was used for data analysis. Although, more refinement would have been helpful, however, due to limited computational resources 10 million was the maximum mesh size computable. Fig. 10

shows a schematic of the front plane of the mesh for the 5 X 5 X 5 geometry.

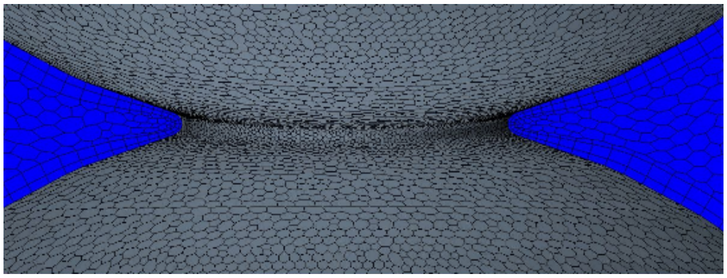

Fig. 9. Sphere contact modification

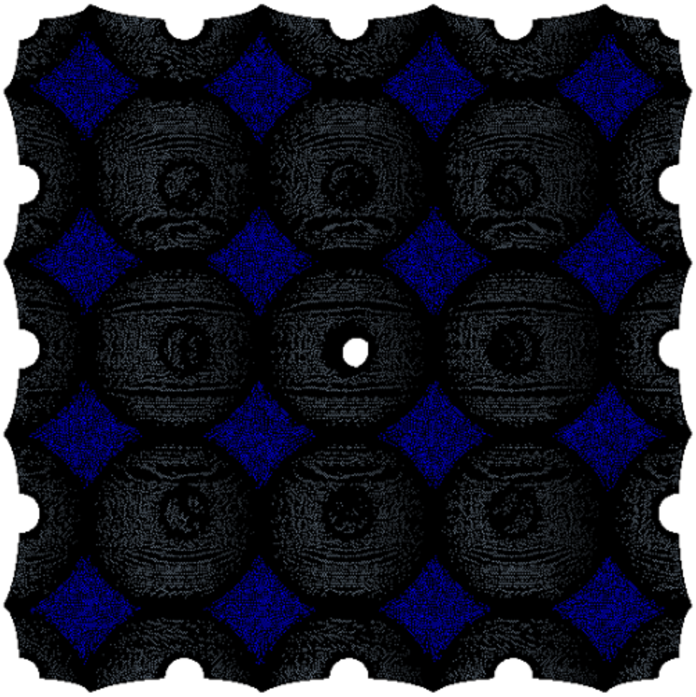

Fig. 10. Front plane mesh scene for simple cubic geometry

For the body centered cubic geometry, same approach was taken for the sphere contact point issue. However, a much more strict and numerically intensive sensitivity analysis was implemented. This is because the body centered geometry is much more complex than the simple cubic geometry. For the body centered case another modification was used on top of the sphere contact point modification. From Fig. 7 we can see the existence of a sphere right above the outlet plane. Now, from fluid mechanics we know about the existence of a wake and the vortex streak in case of flow past a sphere. This phenomenon resulted in reversed flow at the outlet boundary condition for the body centered cubic geometry. To avoid any numerical error in the pressure drop calculation of the computational test section, an extrusion region was added after the outlet. An extrusion is a technique of using the outlet plane mesh and creating a vertical elongation of that outlet mesh face. Fig. 11 shows the initial mesh and the modified mesh with the added extrusion region.

Only three polyhedral meshes was made for the body centered cubic geometry, because the mesh size for body centered case the mesh size increase rapidly with a small decrease in base size. Table IV shows the specification for all the three meshes used for body centered cubic sensitivity analysis.

Table IV. Body Centered Cubic Meshes

Mesh Number	Pebble Region	Total Region
1	4,829,682	5,629,662
2	7,862,464	10,487,464
3	14,483,694	18,366,414

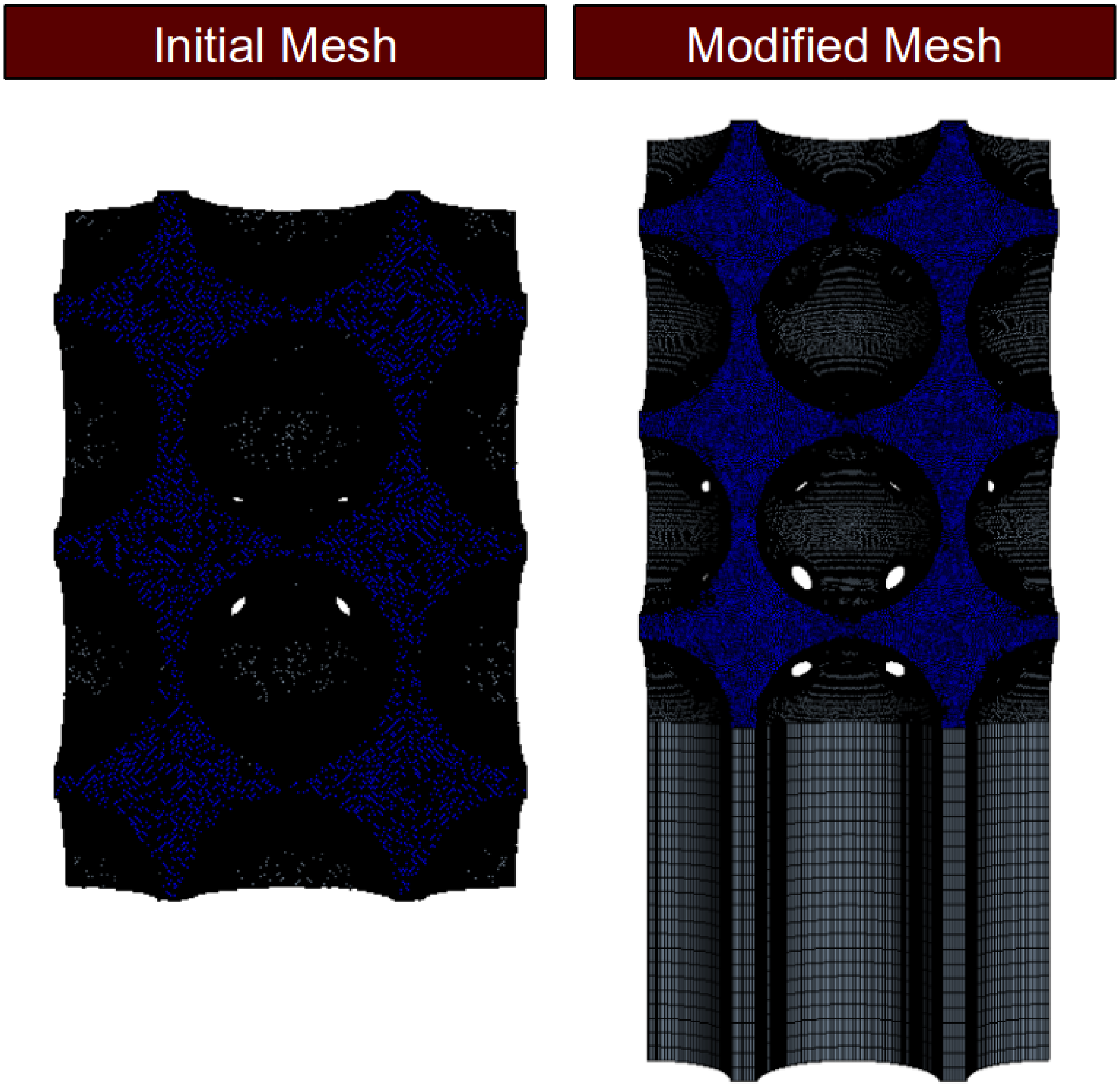

Fig. 11. Front plane mesh scene for body centered cubic geometry

Table 4 has the two columns referred to as “Pebble Region” and “Total Region”. Pebble region represents the initial mesh shown in Fig. 11 where as the total region represents the modified mesh in Fig. 11.

All the three meshes for the body centered cubic geometry have five prism layers for close the the wall treatment. See Appendix for the images of a plane of the volume mesh for the three meshes for body centered case. It shows a difference in the polyhedral cell size for all the three meshes. Fig. 12 shows the prism layers from the third mesh that has the largest number of cells.

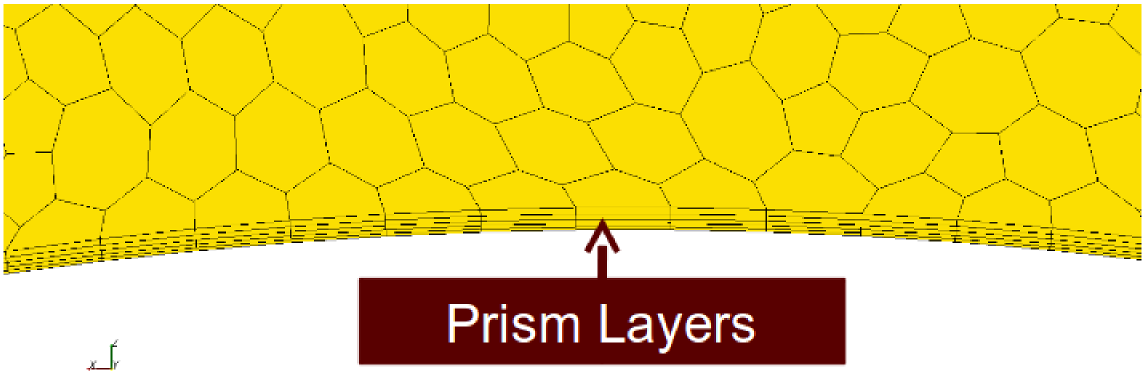

Fig. 12. Prism layers in the body centered cubic geometry

For the mesh sensitivity for the body centered cubic geometry Richardson extrapolation method specified by Celik was used. [13]

Two fluid flow parameters that were used for sensitivity analysis of the three meshes. These parameters were analyzed over a plane at multiple heights of the test section. The parameters used for sensitivity study were:

1. Area averaged Pressure
2. Total vorticity

Table V shows some of the reporting parameters that are specified by Celik. [13]

Table V. Grid Refinement Ratio

Mesh	Mesh Size	Grid Size	Cell Ratio
1	5,629,662	0.62	1.18
2	10,487,464	0.53	1.23
3	18,366,414	0.43	

The last column in the table above represents the average mesh size ratio. This ratio is recommended to have a value greater than or equal to 1.3. [13] However, that number is for structured meshes, whereas in this study, all the meshes were unstructured. In fact, obtaining a structured mesh for the body centered cubic geometry would have been extremely difficult.

As mentioned above, two sensitivity parameters were considered in this study. Area averaged pressure for the body centered cubic geometry showed oscillatory convergence. Fig. 13 shows the area averaged pressure data at different vertical positions for all the three polyhedral meshes.

From Fig. 13, it can be seen that for the highest mesh the pressure curve has a decreasing oscillatory trend which is best captured by the finest mesh. This oscillatory behavior for flow properties is expected in a geometry comprised of spheres.

Table VI shows some important numerical uncertainty values for area averaged pressure parameter. Apparent order represents the numerical order of convergence of the numerical solution for a particular parameter. Grid Convergence Index (GCI) represents the numerical uncertainty associated with the fine grid in comparison to the lower resolution grid. It is important to note that this uncertainty analysis does not have anything to do with the physical meaning of the solution. [13] It is strictly a numerical scheme to analyze the effect of grid refinement on the final solution of any particular equation.

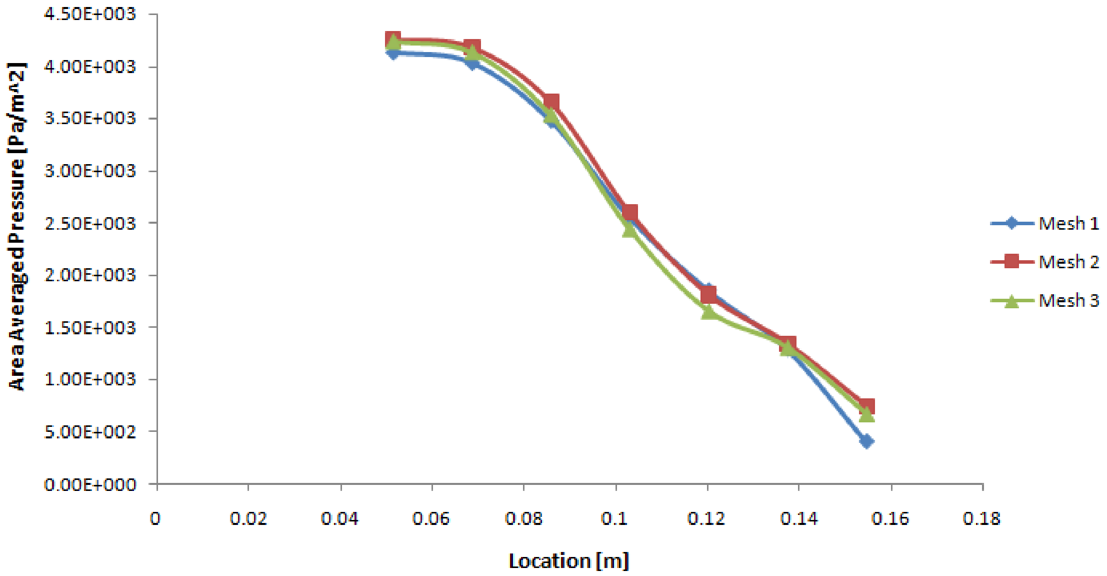

Fig. 13. Area averaged pressure sensitivity

Table VI. Area Averaged Pressure Sensitivity

Property	Value
Apparent order	8.69
GCI-21	0.76 %
GCI-32	2.25 %

On the other hand, the total vorticity parameter showed normal convergence. The plot for the total vorticity data is shown in Fig. 14

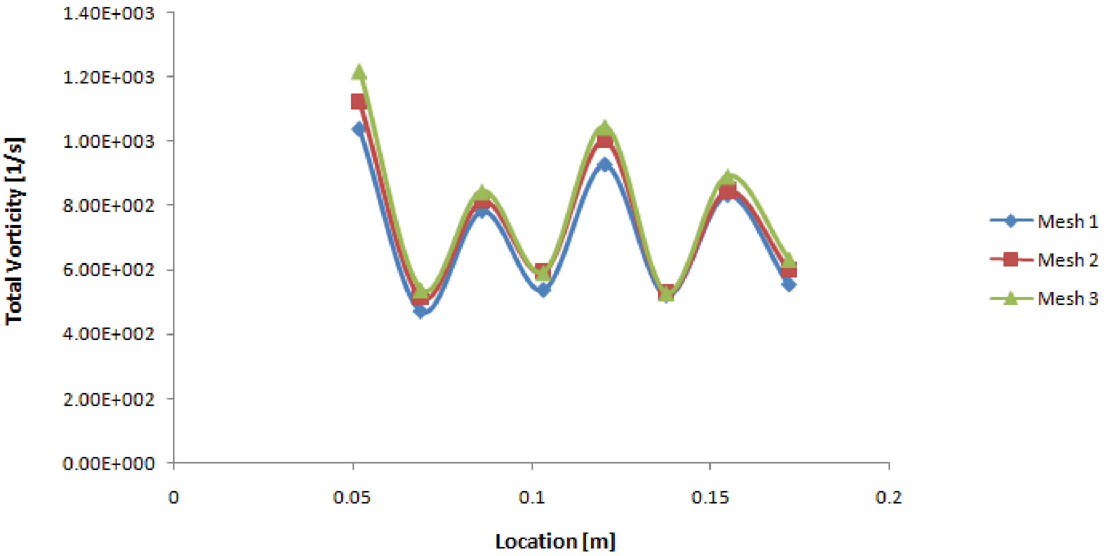

Fig. 14. Total vorticity sensitivity

Table VII contains the reporting parameters for the total vorticity parameter that quantify numerical uncertainty for total vorticity. According to Richardson extrapolation method the most refined mesh has a numerical uncertainty of 4.5 % in the total vorticity parameter.

Table VII. Total Vorticity Sensitivity

Property	Value
Apparent order	6.79
GCI-21	54.0 %
GCI-32	4.54 %

C. Physics Continuum

For both, the simple cubic case and the body centered cubic case, five different modified Reynolds numbers were modeled. Mathematical representation of modified Reynolds number is shown in the Eq. 3.2.

$$Re_m = \frac{Re}{1 - \eta} \tag{3.2}$$

Using this modified Reynolds Number, fluid's superficial velocity was determined. Superficial velocity refers to fluid velocity with no spheres. From there using conservation of mass the computational inlet velocity of the fluid was determined. These model inlet velocities for both the cases are shown in Tables VIII and IX.

Table VIII. Simple Cubic Inlet Velocities

Modified Reynolds Number	Simple Cubic	
	Superficial Velocity [m/s]	Inlet Velocity [m/s]
10,000	0.082	0.43
20,000	0.163	0.86
30,000	0.245	1.29
40,000	0.327	1.71
50,000	0.409	2.14

For all the test cases, water was used as the working fluid. In this study we computationally analyzed the pressure drop at high Reynolds number, that is why water was used as a working fluid as opposed to Helium. With the density of fluid we would have supersonic flow velocities and which we wanted to avoid. This is different from the actual reactor, however, the main purpose of this study was to conduct fluid flow analysis and thus for convenience water was chosen. All the test cases were isothermal and constant properties were used for water.

Table IX. Simple Cubic Inlet Velocities

Modified Reynolds Number	Body Centered Cubic	
	Superficial Velocity [m/s]	Inlet Velocity [m/s]
10,000	0.010	0.258
20,000	0.210	0.516
30,000	0.310	0.774
40,000	0.410	1.03
50,000	0.520	1.29

For the outlet boundary condition, a pressure outlet boundary condition was used with pressure at the outlet face being 0 Pascals(gage pressure). All the sides of the test section, shown in Fig. 8 and 5, had symmetry plane boundary conditions. All the walls had no-slip and no penetration boundary condition. Finally, all the modeled test cases were steady state.

CHAPTER IV

TURBULENCE THEORY

In this study we used RANS based models, namely Realizable k-epsilon model and Reynolds Stress transport model for the fluid flow analysis. In this section various models in this categories are discussed. By the end of this section it will be clear as to why the two models were studied as opposed to other RANS and RST models.

Turbulence in itself is an extremely complicated coupled process. So in order to understand turbulence analytically, major assumptions must be made to simplify the actual phenomenon. We start with the Navier Stokes Equation shown in Eq.4.1 that represents a complete description of the forces that act on a fluid control volume.

$$\frac{DU_j}{Dt} = \frac{\partial U_j}{\partial t} + U_i \frac{\partial U_j}{\partial x_i} = -\frac{1}{\rho}\frac{\partial P}{\partial x_j} + \mu \frac{\partial^2 U_j}{\partial x_i \partial x_i} \tag{4.1}$$

Eq. 4.1 represents the total velocity which described the fluid flow physics in both, laminar and turbulent flows. The complete equation contains a lot of information making it extremely difficult to analyze the effect of a particular phenomenon, especially in turbulent flows. Unfortunately, majority of flow flied that are encountered in the real world are turbulent in nature. Therefore, a lot of research work currently is focused towards turbulence modeling. There are two ways to solve/estimate turbulence characteristics in a flow field, namely, modeling and simulating. Modeling, refers to solving simplified version of equations that make computation easier. Simulation on the other hand, solves the complete equations and generates a lot of information. Modeling and simulating turbulence both have their advantages and disadvantages. The biggest advantage of turbulence modeling is that its computational cost is negligible when compared with that of simulation. On the other side, the biggest disadvantage of modeling is that it does not solve the complete fluid flow physics and thus does not produce accurate results, as opposed to simulation. There are many existing turbulence models that are based of Reynolds Averaged Navier Stokes (RANS) equation, shown below:

1. Turbulent viscosity models
    (a) Algebraic Models
    (b) One Equation Models
    (c) Two Equation Models
2. Reynolds Stress Transport (RST) Model

On the other hand, there are three other types of simulations that are used quite often for research activities, namely:

1. Large Eddy Simulation (LES)
2. Detached Eddy Simulation (DES)
3. Direct Numerical Simulation (DNS)

For the modeling approach, Eq. 4.1 is simplified using a mathematical technique called Reynolds decomposition. Using this technique, the total velocity in turbulent flows can be divided into two different components,namely, a mean and a fluctuating component as shown in Eq.4.2.

$$U(x,y,z,t) = \overline{U(x,y,z,t)} + u'(x,y,z,t) \tag{4.2}$$

In Eq. 4.2 the first term on the right hand side represents the mean velocity which can be mathematically written as shown below:

$$\overline{U} = \lim_{\triangle t \to \infty} \frac{1}{\triangle t} \int_{t}^{t+\triangle t} U \, dt \tag{4.3}$$

Applying Reynolds decomposition to Eq. 4.1 we can re-write the resulting equation as shown in Eq.4.4.

$$\frac{D(\overline{U_j}+u_j)}{Dt} = -\frac{1}{\rho}\frac{\partial(\overline{P}+p)}{\partial x_j} + \mu\frac{\partial^2(\overline{U_j}+u_j)}{\partial x_i \partial x_i} \tag{4.4}$$

In Eq. 4.4 the left hand side represents the material or total derivative of the total velocity. Eq. 4.5 shows the two terms that make up the total derivative. The first term in the right hand side of Eq. 4.5 represents the local part of their derivative and the second term represents the convective part.

$$\frac{D(\overline{U_j}+u_j)}{Dt} = \frac{\partial(\overline{U_j}+u_j)}{\partial t} + (\overline{U_i}+u_i)\frac{\partial(\overline{U_j}+u_j)}{\partial x_i} \tag{4.5}$$

Eq. 4.4, the form that it is in, completely describes all the physics in a turbulent flow where $\overline{U}$ represents the mean velocity and u represents the fluctuating part. In order to obtain RANS equation we need to take a time integral of Eq. 4.4.

Simplifying Eq. 4.4 and taking the time integral we obtain the RANS equation as shown in Eq.4.6.

$$\frac{\partial\overline{U_j}}{\partial t} + \overline{U_i}\frac{\partial\overline{U_j}}{\partial x_i} + \frac{\partial\overline{u_i u_j}}{\partial x_i} = -\frac{1}{\rho}\frac{\partial\overline{P}}{\partial x_j} + \mu\frac{\partial^2\overline{U_j}}{\partial x_i \partial x_i} \tag{4.6}$$

In the RANS models the mean velocity effects are completely resolved, however the effect of the fluctuating velocity are modeled. On the other hand, LES and DES resolves most of the flow and requires modeling for a small portion. Finally, DNS solves Eq. 4.1 without any changes and resolves the entire energy spectrum of the flow field. It is most expensive out of all the models and other simulations. The lower the amount of modeling, higher the accuracy and the computational cost of the method. However, for the present study we analyzed only RANS based turbulence models and these will be explained in detail.

A. Reynolds Averaged Navier Stokes

RANS models are constructed from Eq. 4.6, which solves for the mean velocity of the fluid. However, Eq. 4.6 requires closure modeling because of the term that is generated from convective acceleration on the left hand side of the equation. For a three dimensional flow, we have four equations that govern the mean velocity field; namely the three velocity equations, and the Poisson Equation. The Poisson equation used here is for the mean pressure.

To obtain Poisson equation, we take the derivative of the Navier Stokes equation shown in Eq. 4.1, as shown in Eq. 4.7. Applying, the continuity equation for incompressible flows shown in Eq. 4.8 to Eq. 4.7 we get the Position equation, Eq. 4.9.

$$\frac{\partial}{\partial x_j}\left(\frac{\partial U_j}{\partial t} + U_i \frac{\partial U_j}{\partial x_i} = -\frac{1}{\rho}\frac{\partial P}{\partial x_j} + \mu \frac{\partial^2 U_j}{\partial x_i \partial x_i}\right) \tag{4.7}$$

$$\frac{\partial U_j}{\partial x_j} = \bigtriangledown \cdot U = 0 \tag{4.8}$$

$$-\frac{1}{\rho} \bigtriangledown^2 P = \frac{\partial U_i}{\partial x_j}\frac{\partial U_j}{\partial x_i} \tag{4.9}$$

The equations Eq. 4.7 to Eq. 4.9 represent the total pressure and total velocity. Applying Reynolds Decomposition to Eq. 4.9 and integrating over time we obtain the Poisson equation for the average pressure, shown in Eq. 4.10.

$$-\frac{1}{\rho} \bigtriangledown^2 \overline{P} = \frac{\partial \overline{U_i}}{\partial x_j}\frac{\partial \overline{U_j}}{\partial x_i} + \frac{\partial^2 \overline{u_i u_j}}{\partial x_i \partial x_j} \tag{4.10}$$

The role of pressure is to enforce continuity ($\partial U_i / \partial x_i$) over the entire flow field. At this point, we have the four equations as mentioned above, however, there are more then four unknowns. The three average velocities, the average pressure and the Reynolds stresses ($\overline{u_i u_j}$) that are generated from taking the time averaging of the Navier Stokes equations. More unknowns than equations presents a *closure problem.* In the current condition, when there are more unknowns than equations, the set of equations are refereed to as *unclosed.* The existence of Reynolds stresses ($\overline{u_i u_j}$) in the RANS equation, Eq. 4.6, need to be resolved or somehow determined in order to solve the posed *closure problem.*

B. Reynolds Stresses

As mentioned above, the Reynolds stresses($\overline{u_i u_j}$) that appear in the RANS equation need to be determined in order to obtain a closed set of equations. A critical review of Reynolds stresses is required in order to resolve the closure problem. From mathematics we know, that Reynolds stresses are components of a second order tensor that is symmetric in nature, which means $\overline{u_i u_j} = \overline{u_j u_i}$). Half of the trace of Reynolds stresses is defined as "turbulent kinetic energy", as shown in Eq. 4.11.

$$k \equiv \frac{1}{2}\overline{u \cdot u} = \frac{1}{2}\overline{u_i u_i} \tag{4.11}$$

Turbulent kinetic energy is the mean specific kinetic energy contained in the fluctuating velocity field. The Reynolds stresses can be separated into two different types of stresses, namely, isotropic part and anisotropic part. The isotropic stresses can be represented by turbulent kinetic energy ($\frac{2}{3}k\delta_{ij}$). The deviatoric anisotropic part can be represented as shown below:

$$a_{ij} \equiv \overline{u_i u_j} - \frac{2}{3}k\delta_{ij} \tag{4.12}$$

So far, the Reynolds stresses have been analyzed mathematically and separated into two parts, isotropic and anisotropic part. However, from a physics perspective the evolution of Reynolds stresses is required and has been studied below. To take a look at the Reynolds stress evolution we start with the fluctuating velocity equation. Fluctuating velocity equation (4.13) is obtained by subtracting the mean velocity equation (Eq. 4.6) from the total velocity equation (Eq. 4.4).

$$\frac{\partial u_j}{\partial t} + \overline{U_i}\frac{\partial u_j}{\partial x_i} = -u_i\frac{\partial \overline{U_j}}{\partial x_i} - \frac{\partial(u_i u_j - \overline{u_i u_j})}{\partial x_i} - \frac{1}{\rho}\frac{\partial p}{\partial x_j} + \mu \bigtriangledown^2 u_j \tag{4.13}$$

At this point making an assumption of homogeneous turbulence we can get rid of $\overline{u_i u_j}$ term in Eq. 4.13 to obtain Eq. 4.14.

$$\frac{\partial u_j}{\partial t} + \overline{U_i}\frac{\partial u_j}{\partial x_i} = -u_i\frac{\partial \overline{U_j}}{\partial x_i} - u_i\frac{\partial u_j}{\partial x_i} - \frac{1}{\rho}\frac{\partial p}{\partial x_j} + \mu \bigtriangledown^2 u_j \tag{4.14}$$

Using convenience of index notation, we can multiply Eq. 4.14 with another fluctuating velocity and using product rule we can obtain Reynolds Stress Evolution Equation (RSEE).

The obtained Reynolds stress evolution equation is shown in Eq. 4.15:

$$\frac{\partial \overline{u_i u_j}}{\partial t} + \overline{U_k}\frac{\overline{u_i u_j}}{\partial x_k} = P_{ij} + \Pi_{ij} + T_{ij} - \varepsilon_{ij} \tag{4.15}$$

where, the four components on the RHS of Eq. 4.15 are Production (shown in Eq. 4.16), Pressure-Strain redistribution(shown in Eq. 4.17), Transport (shown in Eq. 4.18) and dissipation (shown in Eq. 4.19) as shown below.

$$P_{ij} = -\overline{u_k u_i}\frac{\partial \overline{U_j}}{\partial x_k} - \overline{u_k u_j}\frac{\partial \overline{U_i}}{\partial x_k} \tag{4.16}$$

$$\Pi_{ij} = \langle p\left(\frac{\partial u_i}{\partial x_j} + \frac{\partial u_j}{\partial x_i}\right)\rangle \tag{4.17}$$

$$T_{ij} = \frac{\partial}{\partial x_k}\left[-\langle pu_i\rangle\delta_{jk} - \langle pu_j\rangle\delta_{ik} + \mu\frac{\partial\langle u_i u_j\rangle}{\partial x_k} - \langle u_i u_j u_k\rangle\right] \tag{4.18}$$

$$\varepsilon_{ij} = 2\nu\langle\frac{\partial u_i}{\partial x_k}\frac{\partial u_j}{\partial x_k}\rangle \tag{4.19}$$

It can be said that turbulence is made of the phenomenons mentioned in Eq. 4.15, shown above. One of the important properties of turbulent flows is the energy cascade effect. Although cascade can not be seen in the RSEE, it implicitly affects the pressure-strain redistribution and the dissipation term. Turbulence on the whole is a combination of linear and non-linear processes acting together. Starting from Eq. 4.15 we can label each parameter as a linear or non-linear process. Physically a linear process would represent interaction between the mean and the fluctuating fields and a non linear process would represent interaction among the fluctuating fields.

There are two inertial processes that take place in turbulence flows, production as shown in Eq. 4.16 is a linear process representing the production of Reynolds Stresses from the mean flow gradients. Cascade on the other hand is a non linear inertial effect that affects the fluctuating fields. The Pressure Strain redistribution term also has two parts, this come from the derivation of the fluctuating pressure. We need the equation for the fluctuating pressure for Eq. 4.17, to get that we can subtract the mean pressure from total pressure,which yields:

$$-\frac{1}{\rho}\bigtriangledown^2 p = 2\frac{\partial\overline{U_i}}{\partial x_j}\frac{\partial u_j}{\partial x_i} + \frac{\partial^2(u_i u_j - \overline{u_i u_j})}{\partial x_i \partial x_j} \tag{4.20}$$

In homogeneous turbulence, the $\overline{u_i u_j}$ term disappears form Eq. 4.20 as it is expected to be the same everywhere. Therefore, we get:

$$-\frac{1}{\rho}\bigtriangledown^2 p = 2\frac{\partial \overline{U_i}}{\partial x_j}\frac{\partial u_j}{\partial x_i} + \frac{\partial^2 u_i u_j}{\partial x_i \partial x_j} \tag{4.21}$$

From Eq. 4.21, we can divide pressure into two different components, namely, rapid component and slow component. The rapid part deals with the interaction between the mean flow and the fluctuating flow making it a linear process whereas the slow part deals with the interaction among fluctuating fields making it a non-linear process.

Same way as the pressure and the inertial effects, dissipation also has two components. One is linear that represents the viscous action in the smallest scales and the other is the non linear process that is indirectly affected my cascade. At this point, with a fairly detailed analysis of Reynolds stress evolution, we can move from turbulence theory to turbulence modeling.

CHAPTER V

TURBULENCE MODELING

In this study only RANS based modeling was conducted, consequently, we will only focus on RANS based models. As mentioned in the turbulence theory section, RANS based turbulence models have two main categories. These are the turbulent viscosity models and then the Reynolds Stress Transport Model. Both of these categories are discussed further in this section. For both these models we will use certain assumptions, ones that apply to all the cases are:

1. Gravitational forces are neglected
2. Buoyancy forces are neglected
3. Isothermal conditions

A. Turbulent Viscosity Models

Turbulent viscosity models solve Eq. 4.6, and uses various models to solve for the unknown Reynolds Stresses ($\overline{u_i u_j}$). All the turbulent viscosity models use turbulent viscosity hypothesis. Starting from the realization that both the mean velocity strain rate shown in Eq. 5.1 and anisotropy tensor, shown in Eq. 4.12, have five independent components. According to the turbulent viscosity hypothesis, these five components are related to each other through the scalar coefficient ν_T.[16]

$$\overline{S_{ij}} = \frac{1}{2}\left(\frac{\partial \overline{U_i}}{\partial x_j} + \frac{\partial \overline{U_j}}{\partial x_i}\right) \tag{5.1}$$

Thus, using turbulent viscosity hypothesis we obtain Eq. 5.2 which relates the anisotropy tensor and the mean velocity strain rate.

$$a_{ij} = -\nu_T \left(\frac{\partial \overline{U_i}}{\partial x_j} + \frac{\partial \overline{U_j}}{\partial x_i} \right) \tag{5.2}$$

Using Eq. 4.12 and Eq. 5.2 we can obtain an equation for the unknown Reynolds Stresses seen in Eq. 5.3, shown below.

$$\overline{u_i u_j} = \frac{2}{3} k \delta_{ij} - \nu_T \left(\frac{\partial \overline{U_i}}{\partial x_j} + \frac{\partial \overline{U_j}}{\partial x_i} \right) \tag{5.3}$$

In the class of turbulent viscosity models there are three main turbulence models that are discussed below.

1. Algebraic Models

Algebraic models are the easiest and have been developed from a macroscopic or thermodynamic standpoint. These models are extremely limited as far as turbulence application is considered. Overall, all the models that fall under this category equate the turbulent viscosity to a characteristic velocity scale and characteristic length scale of the mean flow, as shown in Eq. 5.4.

$$\nu_T = Constant * (l^* u^*) \tag{5.4}$$

One of the most popular algebraic models is the Prandtl mixing-length model. For the Prandtl mixing-length model the characteristic length scale, l^*, is referred to as mixing length ,l_m, and the characteristic velocity as shown below.

$$u^* = l_m \left| \frac{\partial U}{\partial y} \right| \tag{5.5}$$

In this representation of the turbulent viscosity, there is a major drawback other than the limited application of such an approach, and that is, the mixing length is unknown and must be specified.

2. One Equation Models

One equation models are improvement of the algebraic models. This class of models introduces a new representation of the characteristic velocity. This is because, the representation used for algebraic models shown in Eq. 5.5 is not correct at all times everywhere in the flow domain. The error in the Eq. 5.5 originates from the fact that that turbulent velocity scale is not necessarily zero when the mean velocity gradient is zero.

In 1940's, Kolmogorov and Prandtl suggested use of turbulent kinetic energy rather than the mean flow gradient for a better turbulence physics representation. They suggested that characteristic velocity be represented as shown in Eq. 5.6,

$$u^* = C * k^{1/2} \tag{5.6}$$

where, C is a constant. Using the new representation of characteristic velocity we get a new turbulent viscosity equation, shown in Eq. 5.7

$$\nu_T = C * k^{1/2} l_m \tag{5.7}$$

The turbulent kinetic energy shown in the equations above is not completely unknown and its evolution equation can be obtained from the fluctuating velocity equation (Eq. 4.14. However, the one equation model has the same issue as the algebraic model, that is the unknown mixing length which needs to be specified by user for modeling purposes.

3. Two Equation Models

Within the category of turbulent viscosity models, two equation models are the most superior and perhaps can be called “complete” because for these models specification of characteristic length is not required. There are multiple two equation models, however, for this study only k-epsilon models were used and they will be discussed in this section. For the k-epsilon model along with Eq. 4.6 two other model transport equations are solved that make up turbulent viscosity. These two quantities are turbulent kinetic energy (κ) and turbulence dissipation rate (ε).

The turbulent viscosity for the k-epsilon models is calculated using Eq. 5.8.

$$\nu_T = C_\mu \frac{k^2}{\varepsilon} \tag{5.8}$$

There are multiple types of k-epsilon models that are shown below:

1. Standard k-epsilon model
2. Realizable k-epsilon model
3. Re-Normalization Group (RNG) k-epsilon model
4. Low Reynolds Number k-epsilon model

To obtain the model equation for turbulent kinetic energy we multiply Eq. 4.14 with u_j and take the time average of the resulting equation.

$$\frac{\partial \kappa}{\partial t} + \overline{U_i}\frac{\partial \kappa}{\partial x_i} + \frac{\partial \frac{1}{2} u_i u_j u_j}{\partial x_i} = -\overline{u_i u_j}\frac{\partial \overline{U_j}}{\partial x_i} + \nu(\overline{u_j \bigtriangledown^2 u_j}) - \frac{1}{\rho}\frac{\partial(\overline{pu_j})}{\partial x_j} \tag{5.9}$$

The viscosity term in the equation above can be simplified as shown below.

$$\nu(\overline{u_j \bigtriangledown^2 u_j}) = 2\nu\frac{\partial}{\partial x_i}(\overline{u_j s_{ij}}) - \varepsilon \tag{5.10}$$

Using the simplification above we obtain the model turbulent kinetic energy equation (Eq. 5.11),

$$\frac{\partial \kappa}{\partial t} + \overline{U_i}\frac{\partial \kappa}{\partial x_i} + \bigtriangledown \cdot T' = P - \varepsilon \tag{5.11}$$

where

$$T' \equiv \frac{1}{2}(\overline{u_i u_j u_j}) + \frac{\overline{p u_i}}{\rho} - 2\nu(\overline{u_j s_{ij}}) \tag{5.12}$$

$$P = -\overline{u_i u_j}(\overline{S_{ij}}) \tag{5.13}$$

$$\varepsilon \equiv 2\nu(\overline{sijs_{ij}}) \tag{5.14}$$

Physically in Eq. 5.11, T' represents the transport of turbulent kinetic energy, P represents turbulent kinetic energy production and ε represents the turbulent kinetic energy dissipation or turbulence dissipation. The turbulent kinetic energy equation in its form shown in Eq. 5.11 has two unknowns, namely, the transport term and the dissipation term. In order to obtain a complete set of differential equations these terms need to be determined.

The transport term is modeled using gradient-diffusion hypothesis as shown below,

$$T' = -\frac{\nu_T}{\sigma_\kappa} \bigtriangledown \kappa \tag{5.15}$$

where the 'turbulent Prandtl number' (σ_k) is generally taken to be 1.0. The turbulent kinetic energy (k) is calculated using the model equation shown above for each of the models in the k-epsilon category. However, the equation has another term that is not known, dissipation which is calculated differently for the multiple k-epsilon models.

Out of the all the k-epsilon models mentioned above, only standard and realizable k-epsilon models were used in this study and these are discussed further.

a. Standard k-epsilon Model

Standard K-epsilon model is a semi-empirical model that uses Eq. 5.8 to calculate turbulent viscosity with C_μ having a constant value of 0.09. The dissipation term (ε) for this model is calculated using a model equation shown in Eq. 5.16. [16]

$$\frac{\partial \varepsilon}{\partial t} + \overline{U_i}\frac{\partial \varepsilon}{\partial x_i} = \nabla \cdot \left(\frac{\nu_T}{\sigma_\varepsilon} \nabla \varepsilon\right) + C_{\varepsilon 1}\frac{P\varepsilon}{\kappa} - C_{\varepsilon 2}\frac{\varepsilon^2}{\kappa} \tag{5.16}$$

The dissipation equation shown above is however not the exact dissipation equation. The effect of dissipation can be viewed as the energy cascade process in turbulence. Or in other words, dissipation represents the energy flow rate from the large flow structures to the small flow structures in a turbulent flow field. Moreover, this dissipation process was determined to be independent of viscosity at high Reynolds number by Kolmogorov. However, the exact equation of dissipation pertains to the process in the dissipative range in a turbulent flow, which represents the effect of viscosity. Therefore, a model equation of dissipation (Eq.5.16) that is entirely empirical is used to determine dissipation rather than the actual equation.

The standard k-epsilon model that solves Eq. 5.11, Eq. 5.16 along with Eq.4.6 and Eq. 5.8 is in a closed form with five unknowns that appear in the model turbulent kinetic energy equation and the dissipation equation.

The standard values of all the model constants due to Launder and Sharma (1974) are $C_\mu = 0.09$, $C_{\varepsilon 1} = 1.44$, $C_{\varepsilon 2} = 1.92$, $\sigma_\kappa = 1.0$, and $\sigma_\varepsilon = 1.3$. [16]

b. Realizable k-epsilon Model

The realizable K-Epsilon model is substantially better than the standard K-Epsilon model for many applications, and can generally be relied upon to give answers that are at least as accurate. [17] The previous statement is made from theoretical point of view because realizable k-epsilon model addresses certain key issues that standard k-epsilon does not. Lets us consider the first component of the Reynolds stresses, Eq. 5.3, shown below.

$$\overline{u_1^2} = \frac{2}{3}k - \nu_T \left(\frac{\partial \overline{U_1}}{\partial y} \right) \tag{5.17}$$

Using the definition of turbulent viscosity used in standard k-epsilon we can re-write the equation above as shown below.

$$\overline{u_1^2} = \frac{2}{3}k - C_\mu \frac{k^2}{\varepsilon} \left(\frac{\partial \overline{U_1}}{\partial y} \right) \tag{5.18}$$

The normal Reynolds stress shown in the equation above, by definition, is a positive term. However for standard k-epsilon it becomes negative for a large mean velocity strain making standard k-epsilon "non-realizable". Realizable k-epsilon accounts for this characteristic of turbulent flows thereby satisfying the "lumley triangle" criteria for all turbulent flows.

One other major issue with standard k-epsilon is the model equation of turbulent dissipation rate, which is re-written for realizable k-epsilon shown in Eq.5.19. Eq. 5.19 is based on dynamic equation of the mean square vorticity fluctuation at large turbulent Reynolds number. [14]

$$\frac{\partial \varepsilon}{\partial t} + \overline{U_i} \frac{\partial \varepsilon}{\partial x_i} = \bigtriangledown \cdot \left(\frac{\nu_T}{\sigma_\varepsilon} \bigtriangledown \varepsilon \right) + C_1 S \varepsilon - C_{\varepsilon 2} \frac{\varepsilon^2}{\kappa + \sqrt{\nu \varepsilon}} \tag{5.19}$$

Comparing Eq. 5.19 with Eq. 5.16, two differences can be observed. First, is the replacement of $C_{\varepsilon 1} \frac{P_\varepsilon}{\kappa}$ term with the $C_1 S \varepsilon$ term. This change is crucial from a numerical as well as physical standpoint. Numerically, this dissipation model will be more robust when used with second-order schemes, since S normally behaves better than Reynolds stresses, especially for cases the case with poor initialization. [14]

Physically, the new term $C_1 S\varepsilon$ in Eq. 5.19, that represents “production” is similar to method proposed by Lumley [15] which is based on the concept of spectral energy transfer. This is more accurate because it represents the process of energy transfer from large scales to small scales, which is what happens from turbulence energy cascade theory. Another change in the dissipation equation is the “destruction” term does not have a singularity problem when the turbulent kinetic energy is zero.

Apart from the dissipation equation, another major difference between the realizable k-epsilon and standard k-epsilon comes in calculation of C_μ in the turbulent viscosity equation, Eq. 5.8. Unlike, standard k-epsilon case, C_μ is not a constant value in the realizable k-epsilon model. It is calculated from the mean flow characteristics and thus is more accurate because it takes the flow characteristics into account. The constant is calculated by taking the mean velocity shear rate, rotation rate into account along the the flow’s angular velocity, turbulent kinetic energy and dissipation rate. The exact function for this constant is shown in the equations below: [16]

$$C_\mu = \frac{1}{A_0 + A_s \frac{\kappa U^*}{\varepsilon}} \tag{5.20}$$

where,

$$A_0 = 4.04 \tag{5.21}$$

$$A_s = \sqrt{(6)} cos \left(\frac{1}{3} cos^{-}1 \left(\sqrt{6} \frac{S_{ij} S_{jk} S_{ki}}{\sqrt{S_{ij} S_{ji}}} \right) \right) \tag{5.22}$$

$$U^* \equiv \sqrt{S_{ij} S_{ij} + \left(\Omega_{ij} - 2\epsilon_{ijk}\omega_k\right)\left(\Omega_{ij} - 2\epsilon_{ijk}\omega_k\right)} \tag{5.23}$$

With these parameter the constant C_μ can be shown to have the value of 0.09 (used for standard k-epsilon case) for inertial sub-layer in boundary layer flows. The realizable k-epsilon is also in closed form with a few constants, namely, $C_{\varepsilon 2} = 1.9$, $\sigma_\kappa = 1.0$, $\sigma_\varepsilon = 1.2$, and $C_1 = max \left[0.43, \frac{\eta}{\eta + 5} \right]; (\eta = S\frac{\kappa}{\varepsilon})$.

B. Reynolds Stress Transport Models

Reynolds Stress Transport model, also known as second-moment closure models, are the most complex turbulence models in the Star-CCM+. [17] Reynolds stress transport models solve the transport equation of the Reynolds stresses, also known as Reynolds Stress Evolution Equation (RSEE), shown in Eq. 4.15. The Reynolds stress transport models inherently account for the effects such as anisotropy due to strong swirling motion, streamline curvature, and rapid changes in strain rate. [17].

In Eq. 4.15 the terms that need to be modeled in order to obtain a closed set of differential equations are, a part of transport term, dissipation term, and perhaps the most difficult, the pressure- strain term.

StarCCM+ has three different Reynolds stress transport models:

1. Linear Pressure Strain
2. Quadratic Pressure Strain
3. Linear Pressure Strain Two-Layer

Out of the three models mentioned above, only the linear pressure strain model will be discussed since only that is used in this analysis. The linear pressure strain model was introduced by Launder, Reece and Rodi. [18].

Out of the three unknowns that need modeling, we look at the transport term first. The transport term as before is modeled using simple gradient diffusion hypothesis, proposed by Daly and Harlow (1970). The simple gradient diffusion as in the case of two equation models assumes isotropic diffusion coefficient, which is a source of errors in both the viscosity model and the Reynolds stress transport model.

The dissipation term is another unknown term in Eq. 4.15 that requires closure modeling. To model the dissipation term an assumption of isotropic dissipation is made. The resulting form is shown in the equation below.

$$2\nu\langle\frac{\partial u_i}{\partial x_k}\frac{\partial u_j}{\partial x_k}\rangle = \frac{2}{3}\delta_{ij}\varepsilon_{ij} \tag{5.24}$$

Although, several experimental studies have shown that turbulence does not remain locally isotropic in the presence of strong strain fields (e.g. Townsend 1954;Uberoi 1957). [18] The turbulence energy dissipation rate is still an unknown and for the the Reynolds stress transport model it is modeled as shown in Eq. 5.25.

$$\frac{D\varepsilon}{Dt} = C_\varepsilon\frac{\partial}{\partial x_k}\left(\frac{\kappa}{\varepsilon}\overline{u_k u_l}\frac{\partial u_l}{\partial x_l}\right) - C_{\varepsilon 1}\frac{\varepsilon}{\kappa}\overline{u_i u_k}\frac{\partial U_i}{\partial x_k} - C_{\varepsilon 2}\frac{\varepsilon^2}{\kappa} \tag{5.25}$$

Eq. 5.25 was introduced by Hanjalic and Launder, the first term on the right hand side of the equation represents the diffusive part of turbulent dissipation rate. The second and third terms on the right side of Eq. 5.25 collectively represent the net effect of the generation of ε due to vortex stretching of turbulent filaments and its destruction by viscous action. However, it was pointed by Rotta, Lumley, and Khajeh-Nouri in the 1970's that Hanjalic and Launder's use of the mean strain rate in Eq. 5.25 was faulty.

At this point, we have discussed modeling of the dissipation term and the transport. One more term required modeling to satisfy the closure problem, and that term is pressure-strain term shown in Eq. 4.17. Launder, Reece, and Rodi, collectively, came up with the idea of splitting the pressure-strain term into three terms, namely, a slow term that represents return to isotropy, a rapid term originating from the rapid distortion theory and a close to the wall (wall reflection) term that was developed from works of Bradshaw (1972), Dr. H.P.A Irwin, Launder, Hanjalic, Reece, and Rodi. The rapid part deals with the interaction between the mean flow and the fluctuating flow making it a linear process whereas the slow part deals with the interaction among fluctuating fields making it a non-linear process.This technique of modeling the three unknowns together is referred to as the “Linear Pressure Strain Model.”

CHAPTER VI

DATA ANALYSIS

A. Simple Cubic Geometry

For the simple cubic geometry, only one realizable k-epsilon turbulence model was analyzed. The overall geometry of the simple cubic design is relatively simple as compared to the body centered cubic geometry.

1. Pressure Drop

From a nuclear reactor design perspective, the pressure drop inside the core of the reactor is an important parameter that requires proper analysis. The computational pressure drop obtained from the computational analysis is compared with two existing famous semi-empirical correlations, namely KTA correlation and Choi correlation. For actual PBMR design KTA correlation was being used for the reactor design. Thus, in this analysis KTA correlation is assumed to be a fairly accurate representation of the pressure drop inside the core. Table X compares the computational pressure drop with the KTA correlation using the porosity of the test section.

Table X. Pressure Drop for Simple Cubic Geometry

Modified Reynolds Number	CFD ΔP	KTA correlation ΔP	% difference
10,000	95.7	55.3	42.2
20,000	355.1	239	32.7
30,000	765.5	554.9	27.5
40,000	1320.8	995.1	24.7
50,000	2016.9	1635.4	18.9

It should be noted that the percent discrepancy between the KTA and and computational pressure drop decreases with an increase in the modified Reynolds number. This decreasing disagreement between the two results occurs due to the applicability of the realizable k-epsilon turbulence model. In other words, according to the pressure drop comparison, for lower modified Reynolds number the realizable K-epsilon two layer turbulence model is not appropriate. Perhaps, the realizable k-epsilon low Reynolds number model should be applied.

This applicability issue of the realizable k-epsilon two layer model for low Reynolds number can be stated with good amount of confidence due to the fact that for low Reynolds number the y+ value for the simulation was determined to be in the range of the log law of the wall region. The log-law of the wall region represents the buffer region in the turbulent boundary layer representation. This implies for further mesh refinement to account for close to the wall effects in the simple cubic geometry. Previous pressure drop results show similar trend for the pressure drop curve. [19] It is also shown that the pressure drop values are close to each other for low Reynolds number and at high Reynolds number the difference increases. This is observed in the computational pressure drop result as well. However, if we take a look at the percent difference, we can see that the low Reynolds number values in fact have more discrepancy. Fig. 15 shows the y+ for the case of 10,000 modified Reynolds number, one can see that the maximum wall y+ for the low Reynolds number is in the range of the buffer region which from turbulence theory, ranges from a y+ value of 5 to 30.

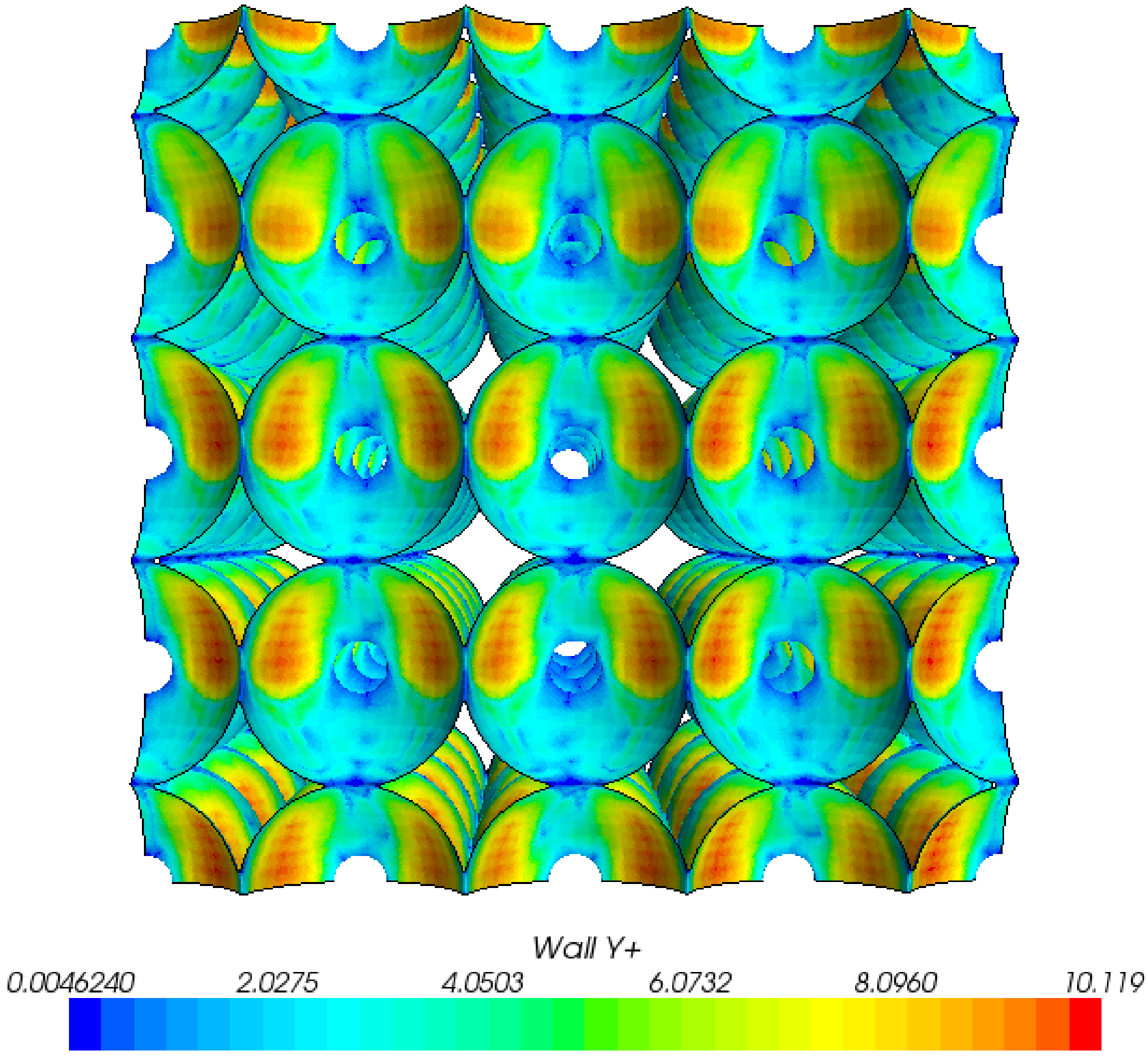

Fig. 15. Simple cubic wall Y+

Fig. 16 shows the pressure drop data for the two correlations and the computational result using the realizable k-epsilon turbulence model. The computational pressure drop for the simple cubic geometry seems to be decent agreement with KTA correlation. However, Choi correlation predicts a higher pressure drop. Regardless, the pressure drop growth with increasing modified Reynolds number seems to have a similar trend, from both the KTA and the computational result.

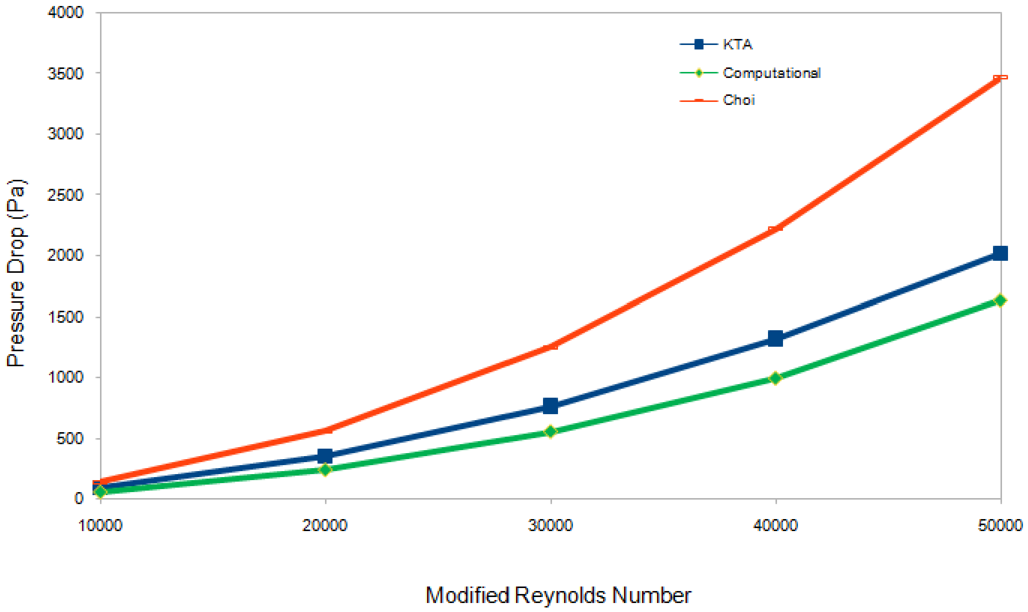

Fig. 16. Simple cubic pressure drop comparison

2. Fluid Flow Analysis

In the PBMR the fluid flow inside the reactor core is strongly dependent on the packing of the spheres, which is random. This makes it hard to predict the flow structure in the PBMR core because of the unknown sphere distribution and the area of contact among the spheres due to complex flow separation. [5] Using the test cases from this study we can determine certain flow features or structure that are expected to exist inside the PBMR core. This is extremely important for the PBMR core from a reactor safety perspective. [4] Each modified Reynolds number showed a different outlet profile as far as the velocity magnitude is concerned. However, the flow structure in each case showed similar features such as vortex formation downstream and between the pebbles due to complex flow separation. Fig. 17 represents the streamlines for one of the simple cubic simulations that shows multiple vortices being formed downstream of the spheres and at sphere contact points.

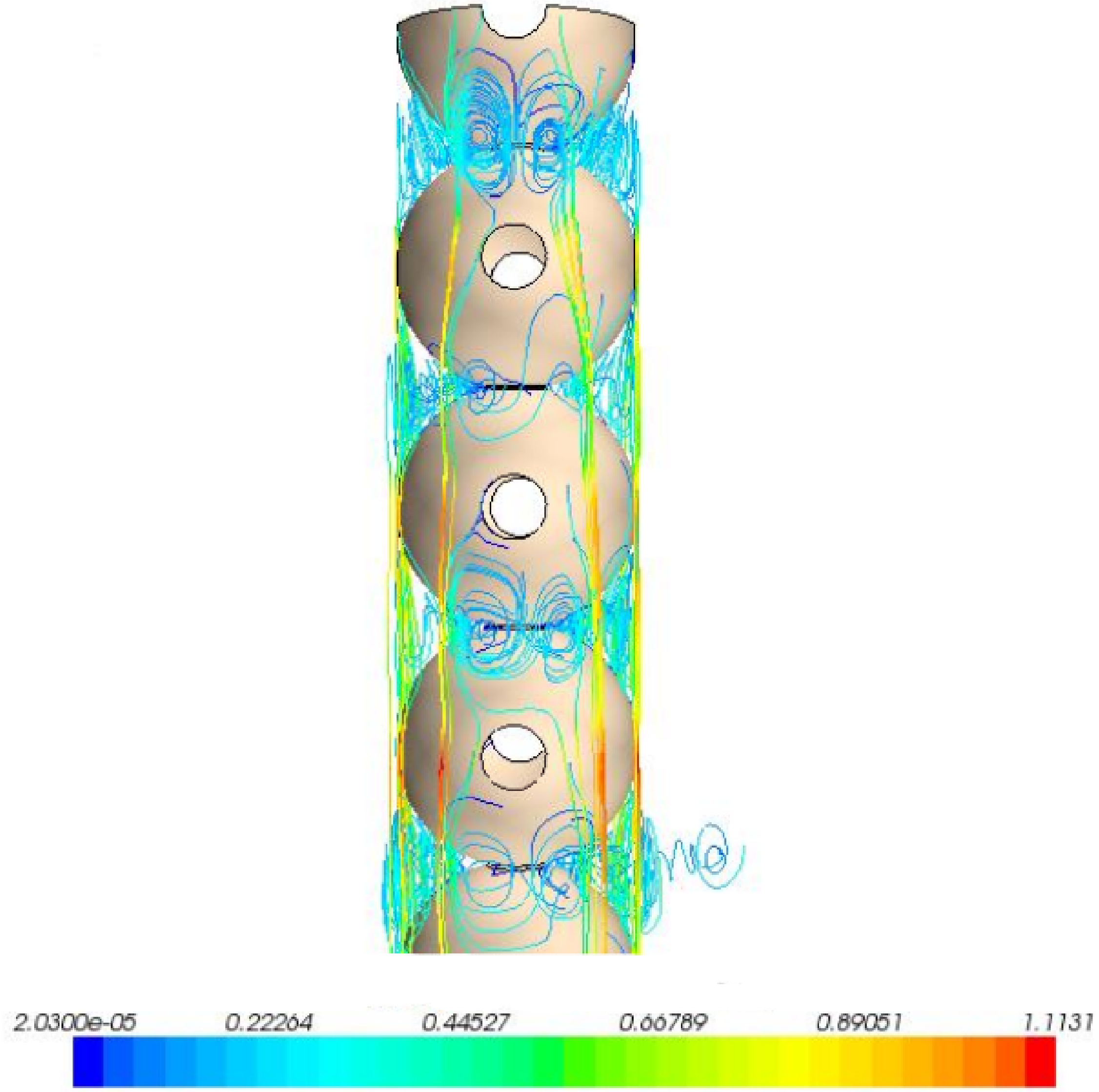

Fig. 17. Fluid flow streamlines in the simple cubic geometry

As far as the fluid flow profile is concerned, for the simple cubic cases the obtained velocity profile was similar to what was expected. Fig. 18 shows the outlet profile for the modified Reynolds number of 10,000.

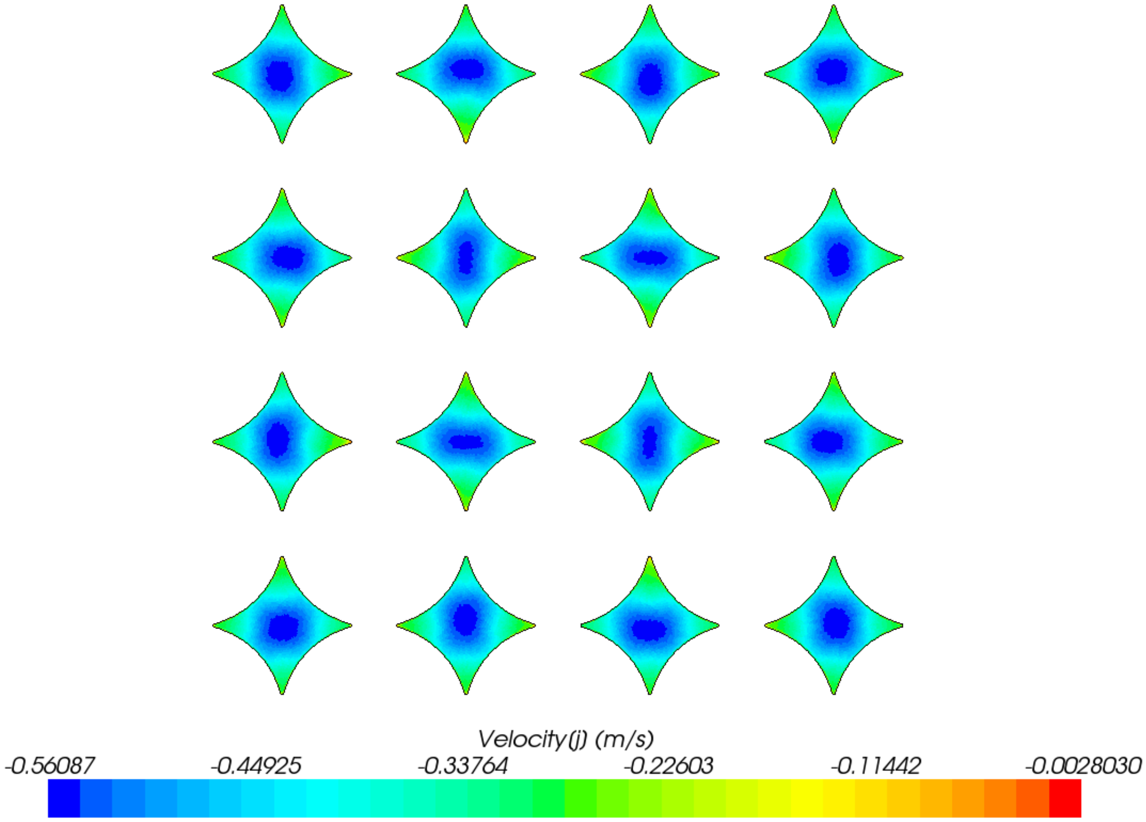

Fig. 18. Outlet flow profile for the simple cubic geometry (Re= 10,000)

It should be noted that the snapshot shown above is for the lowest Reynolds number case. There is a distinct pattern in the flow profile for each of the “outlet channels”. However, with increasing Reynolds number this pattern disappears and all the channels look the same as shown in Fig. 19

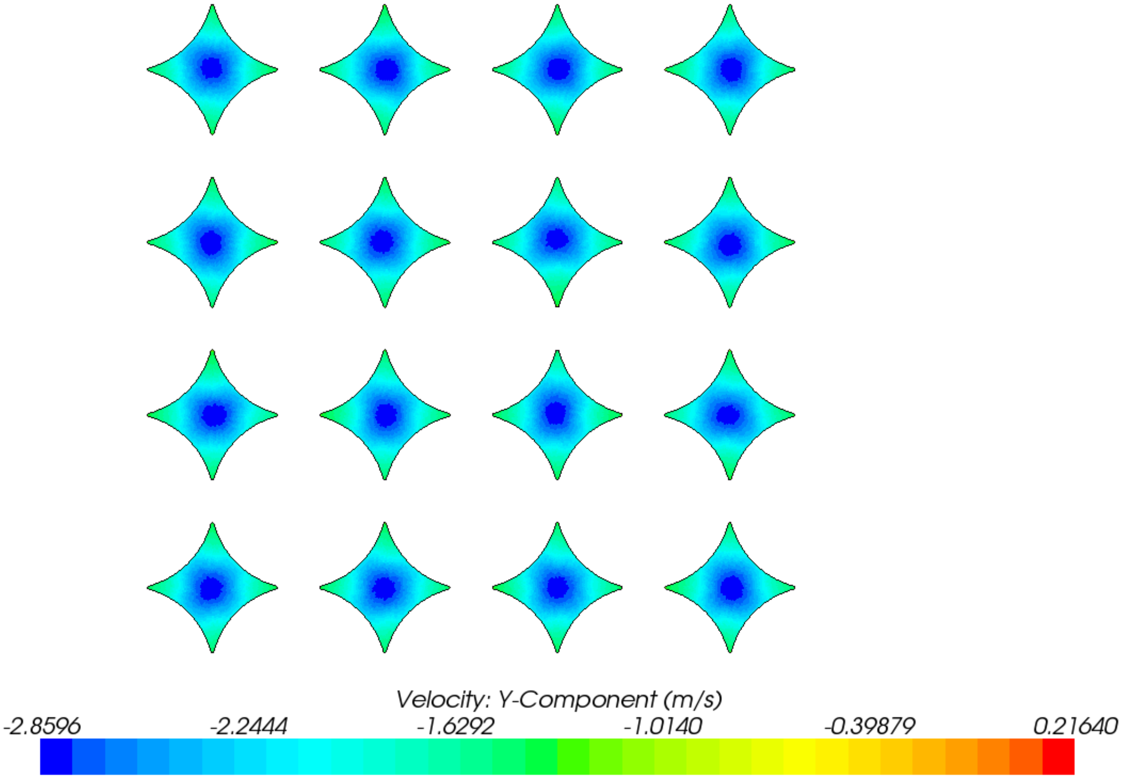

Fig. 19. Outlet flow profile for the simple cubic geometry (Re= 50,000)

B. Body Centered Cubic Geometry

For the body centered cubic geometry, three turbulence models were used, namely, standard k-epsilon, realizable k-epsilon, and Reynolds stress transport model. The body centered cubic geometry is much more complex as compared to the simple cubic geometry. It will be seen further in this section that the choice of turbulence model is extremely crucial for a geometry like the body centered cubic.

1. Pressure Drop

For the pressure drop calculation, the standard and the realizable k-epsilon were modeled for all the Reynolds number. However, the Reynolds stress transport model was was only used for the highest Reynolds number case. This is due to the fact that Reynolds Stress transport model is extremely expensive and has a big computational time cost associated with it. Table XI compares the standard k-epsilon and the realizable k-epsilon pressure drop result with the KTA correlation. In the table below, SKE represents standard k-epsilon and RKE represents realizable k-epsilon turbulence model.

Table XI. Pressure Drop for Body Centered Cubic Geometry

Modified Reynolds Number	SKE ΔP	RKE ΔP	KTA ΔP
10,000	274.51	165.39	651.24
20,000	718.60	1248.00	2415.58
30,000	2156.69	1396.49	5207.72
40,000	2582.52	2288.4	8985.45
50,000	5756.29	7340.37	13720.4

The pressure drop obtained from the Reynolds stress transport model for the modified Reynolds number of 50,000 was in between the realizable k-epsilon and the standard k-epsilon with a value of 5878.50 Pascals. Unlike the simple cubic geometry, the pressure drop comparison with the KTA correlation is not in good agreement with the KTA result. In fact, the body centered cubic result is very different from that of KTA's. The percent difference from the KTA pressure drop also does not have any order like in the case of simple cubic. This is because the geometry is much more complex than the simple cubic geometry. In fact, the body centered cubic geometry has a lot of contractions and expansions creating a lot of mean flow strain and realizable k-epsilon has proved to be not good for such flows. [16]

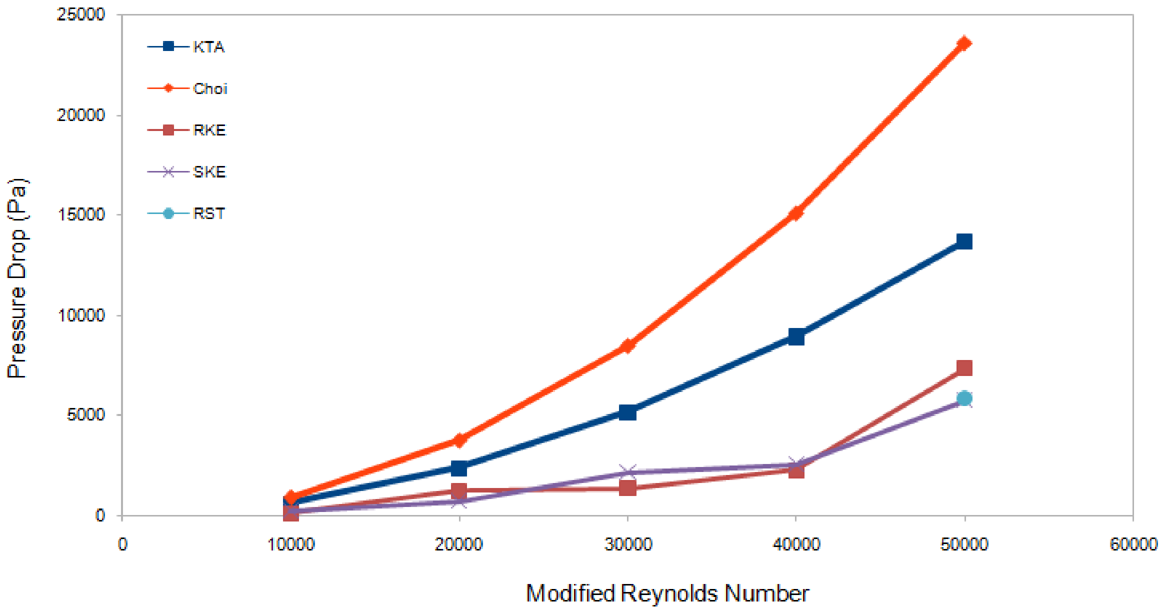

Fig. 20. Pressure drop for body centered cubic geometry

Fig. 20 graphically compares the computational result with KTA and Choi correlations. From Fig. 20 it is clear that the computational result for the body centered cubic geometry has some significant sources of error or assumptions that are not appropriate for this case. Numerical error is one source which was analyzed in the mesh sensitivity section of this report and error due to choice of turbulence model is another major error that is discussed later in this section.

As mentioned previously, the flow parameters inside the PBMR core is highly dependent on the porosity of the core. This is confirmed from Fig. 21, that shows the realizable k-epsilon result for both the cases. Before the analysis a hypothesis was made regarding the relation of porosity with the flow parameter. Basically, it was stated that higher the porosity the lower the flow parameter value and vice-versa. This statement is confirmed by the result shown in Fig. 21 that compares the pressure drop for two geometries with different porosity. The number in the legend in Fig. 21 represents the porosity of that specific geometry.

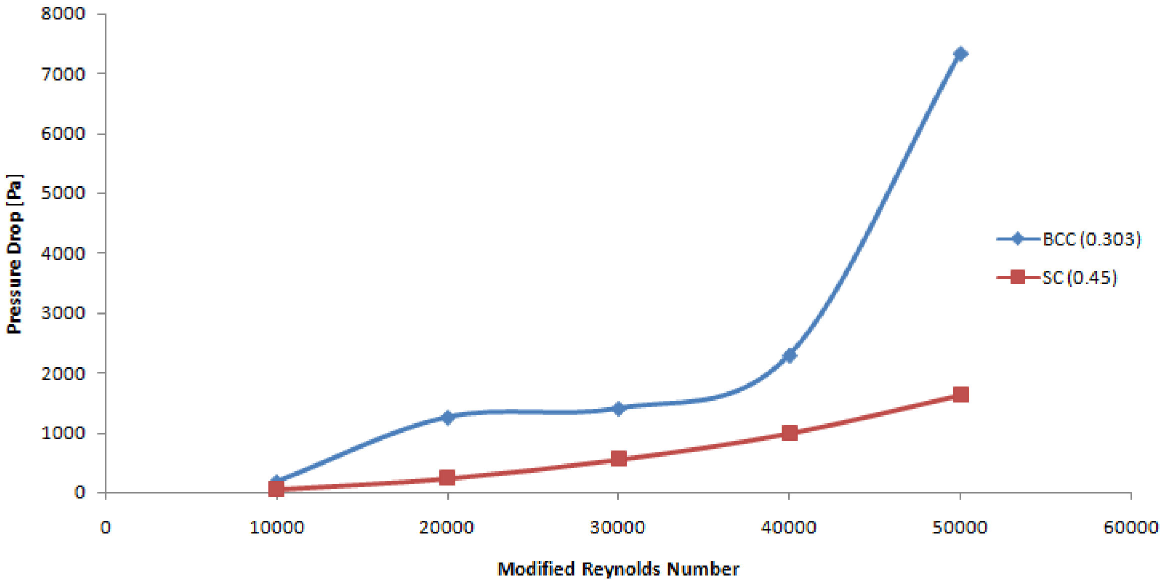

Fig. 21. Porosity effect

2. Fluid Flow Analysis

The fluid flow in the case of body centered cubic geometry demonstrated similar features as the simple cubic geometry and what as been seen before, that is the formation of multiple vortices. This is very important flow feature that needs thorough analysis, ince it can lead to formation of hot spots in a in the actual core.

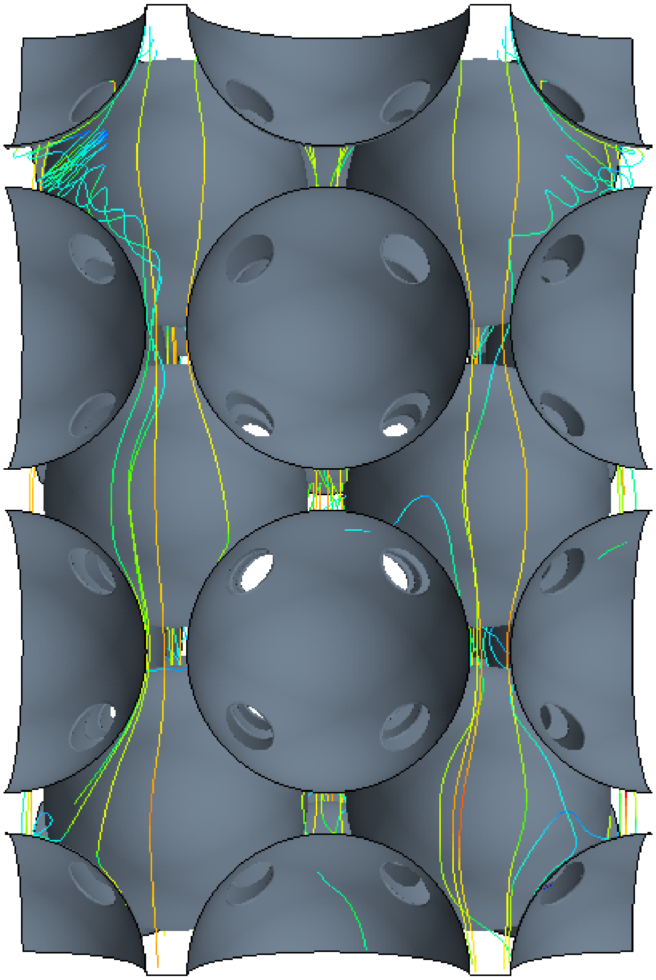

Fig. 22. Streamlines for body centered cubic geometry

Moreover, with increasing operating time it can also lead to phenomena such as particle deposition. This is a big issue from a reactor safety perspective, especially, since it can hinder the material integrity of the fuel spheres inside the core. Fig. 22 shows the streamlines in the body centered cubic geometry that shows favorable vortex formation locations in the body centered cubic geometry.

Although, all the turbulence models showed similar flow structure, such as formation of vortices downstream of the spheres and high vorticity, they all have very different flow profile.

a. Turbulence Model Comparison

The choice of turbulence model for the body centered geometry seems to be extremely crucial especially from the velocity profile that is obtained from each of the models used in the study. Figs. 23, 24 and 25 shows that outlet velocity profile for the standard k-epsilon, realizable k-epsilon, Reynolds stress transport model.

Comparing the three images one can see that there is a big difference in the fluid flow profile at the outlet for the same geometry for the three turbulence models. Determining the fluid flow in the reactor core is important not only from a safety standpoint, but also from a thermal efficiency perspective. A correct fluid flow profile would enable proper heat transfer calculations and finally in design modifications that would increase the overall efficiency of the reactor.

Now without commenting on which model is the most appropriate of such a analysis, and considering the body centered geometry, certain key comments regarding the expected flow profile can be made. First of all, the body centered cubic geometry has four symmetry boundary conditions, secondly, along the center axis there exists a symmetry in the geometry. From the given information it is a conservative statement to make that the fluid flow on a plane at any vertical height in the test section should have an antisymmetric fluid flow profile. With this hypothesis about the expected

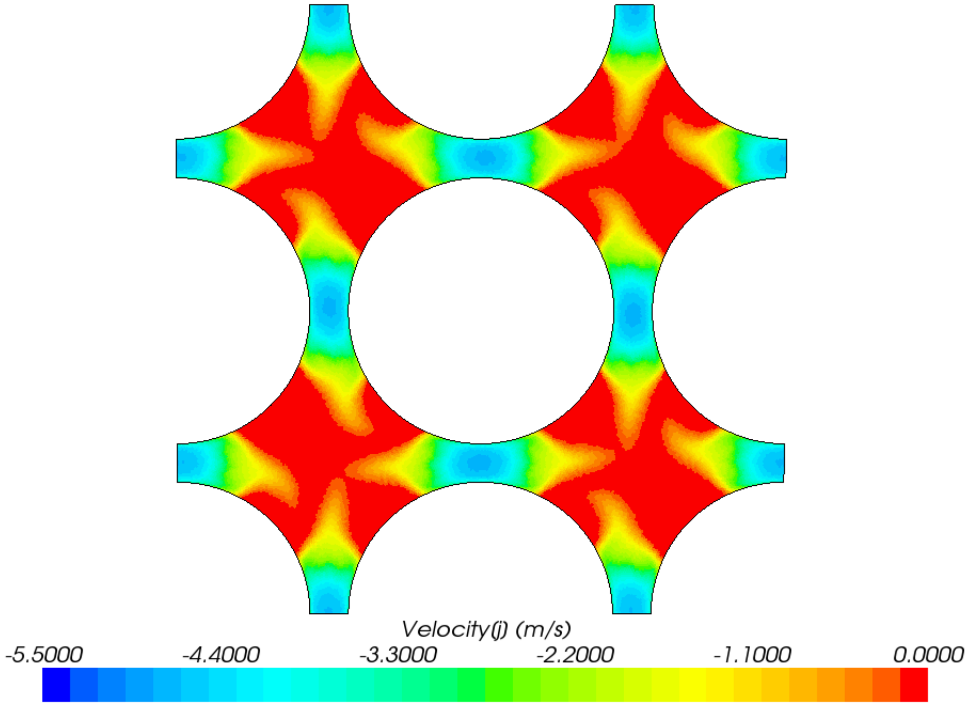

Fig. 23. Outlet velocity profile for body centered cubic geometry - Standard K-epsilon

fluid flow profile as the background information the analysis of the three turbulence models was conducted.

Fig. 23 shows the outlet profile for standard k-epsilon case and it does produce an outlet profile which is axisymmetric in nature. However, from the turbulence theory section we know that standard k-epsilon model is the most basic model that is considered in this analysis. In fact, it ignores most of the turbulence physics and uses equations for dissipation that has many significant drawbacks.

Fig. 26 shows the vector field at the outlet, here it can be noted that the flow is basically coming out of the test section in a straight pattern. In other words, the phenomenon of existence of vortices or wake formation in the case of flow around a sphere is missing for the standard k-epsilon turbulence model. This indicates a major flaw in standard k-epsilon model for the body centered cubic geometry or any similar

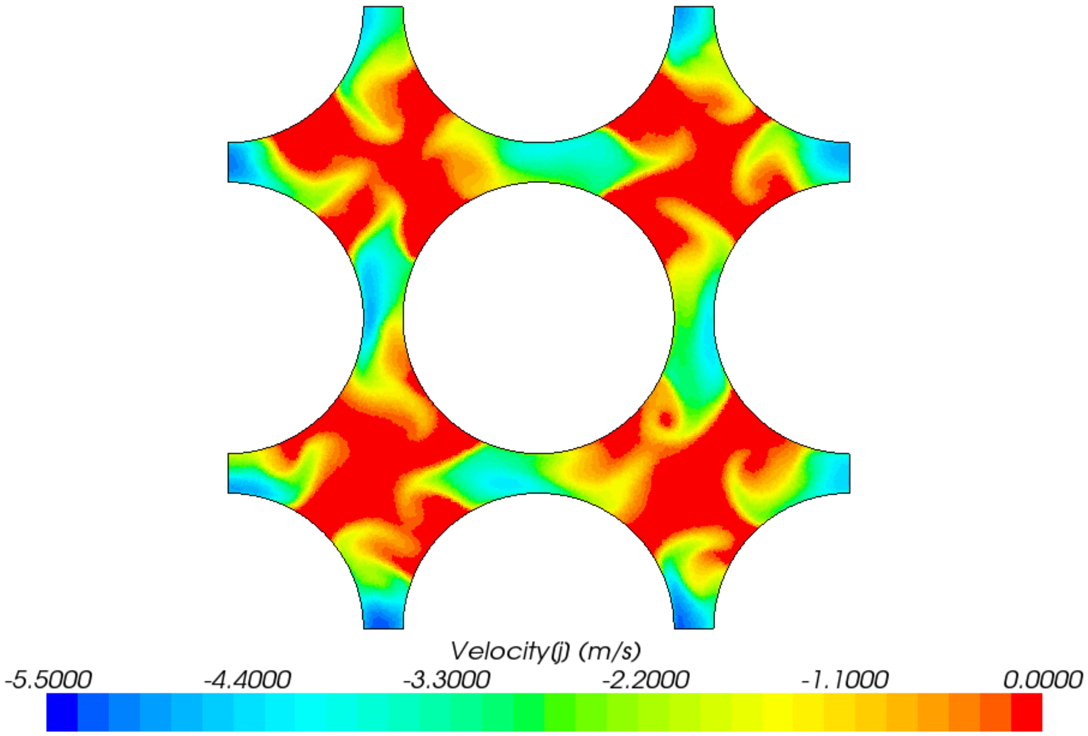

Fig. 24. Outlet velocity profile for body centered cubic geometry - Realizable K-epsilon geometry.

On the other hand the realizable k-epsilon turbulence model, seems to have an extremely distorted outlet velocity profile. In fact, it does not seem symmetric at all, according to Fig. 24. Fig. 27 shows the vector scene of the outlet velocity profile.

In this representation of the velocity profile we can see the existence of multiple vortices that are expected in flow around spheres. However, the velocity profile itself suggests that the realizable k-epsilon model is not fit for such a geometry because it fail to produce the expected velocity profile. Perhaps, it over exaggerates the vorticity in the fluid domain. This is perhaps due to the use of the modified dissipation equation that is used in realizable k-epsilon model that is based from the dynamic vorticity equation.

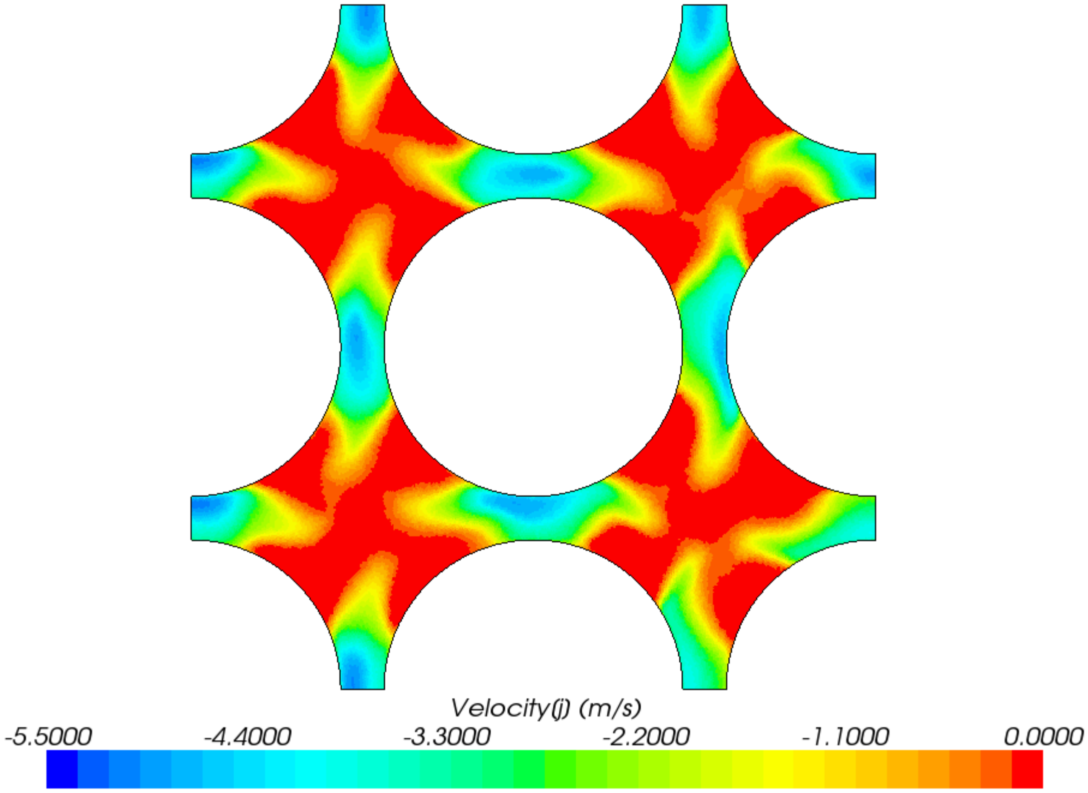

Fig. 25. Outlet velocity profile for body centered cubic geometry - Reynolds Stress

Finally, the outlet velocity profile for the Reynolds stress transport model is shown in Fig. 25. This velocity profile seems to have axisymmetry around the center axis line. Fig. 28 shows the vector scene of the velocity profile at the outlet of the geometry.

The Reynolds stress transport model is the most expensive model. In fact, it accounts for the maximum amount to turbulence physics out of all the models that were used in this study. Fig. 28 shows the swirling in the flow that we have mentioned earlier in this report. At this point, the Reynolds stress transport model seems to model the fluid flow in the geometry fairly well. However, the pressure drop data for the Reynolds stress transport model is very similar to the other computational

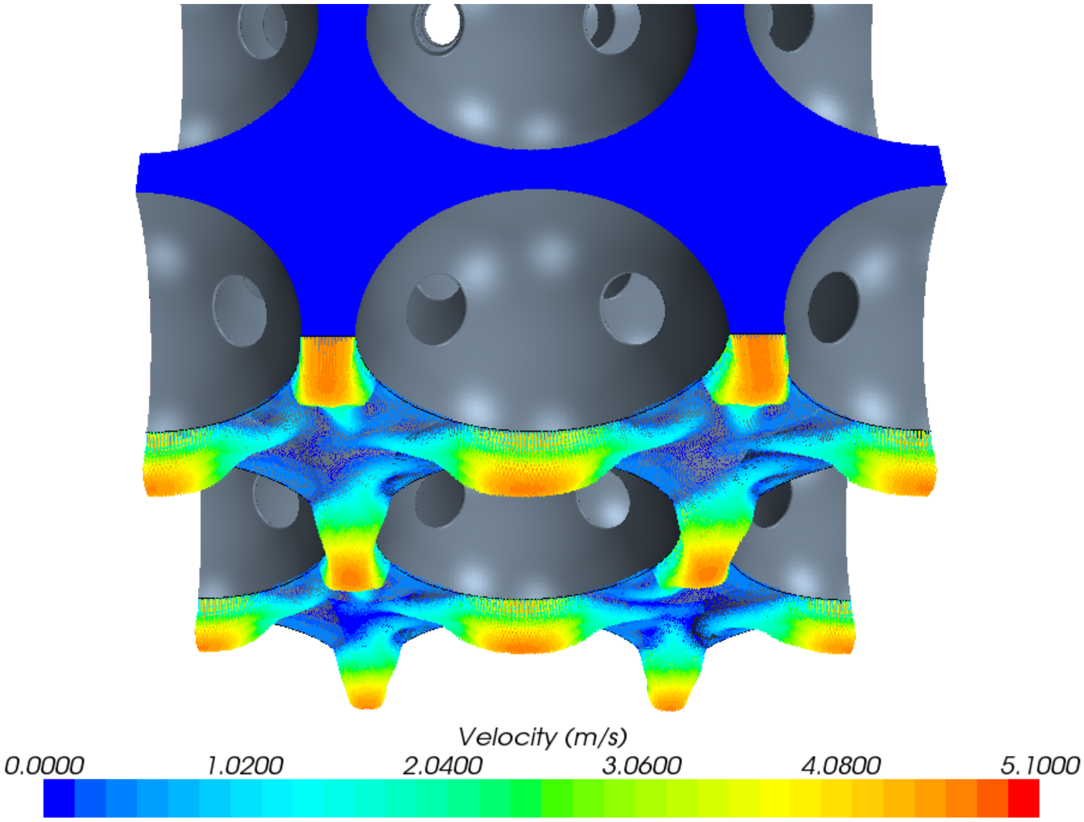

Fig. 26. Velocity vector for the standard k-epsilon model

models used in this study and they are all far from KTA correlation. This is because the Reynolds stress transport model has some errors due the the linear pressure strain redistribution method that is used in this analysis. More specifically, it it the slow pressure term in the pressure-strain redistribution in the Reynolds stress evolution equation, shown in the theory section of this report. This error is because the slow pressure term is developed from the return to isotropy theory and use of this is not appropriate in our analysis due to existence of all the sphere walls in the fluid domain. According to Pope, the redistribution term actually plays a big role, in fact about 60 % in flow energy redistribution. [16] Thus, error due to this particular term can be seen in the pressure drop data that is shown in the Fig. 20. Moreover, it is fair

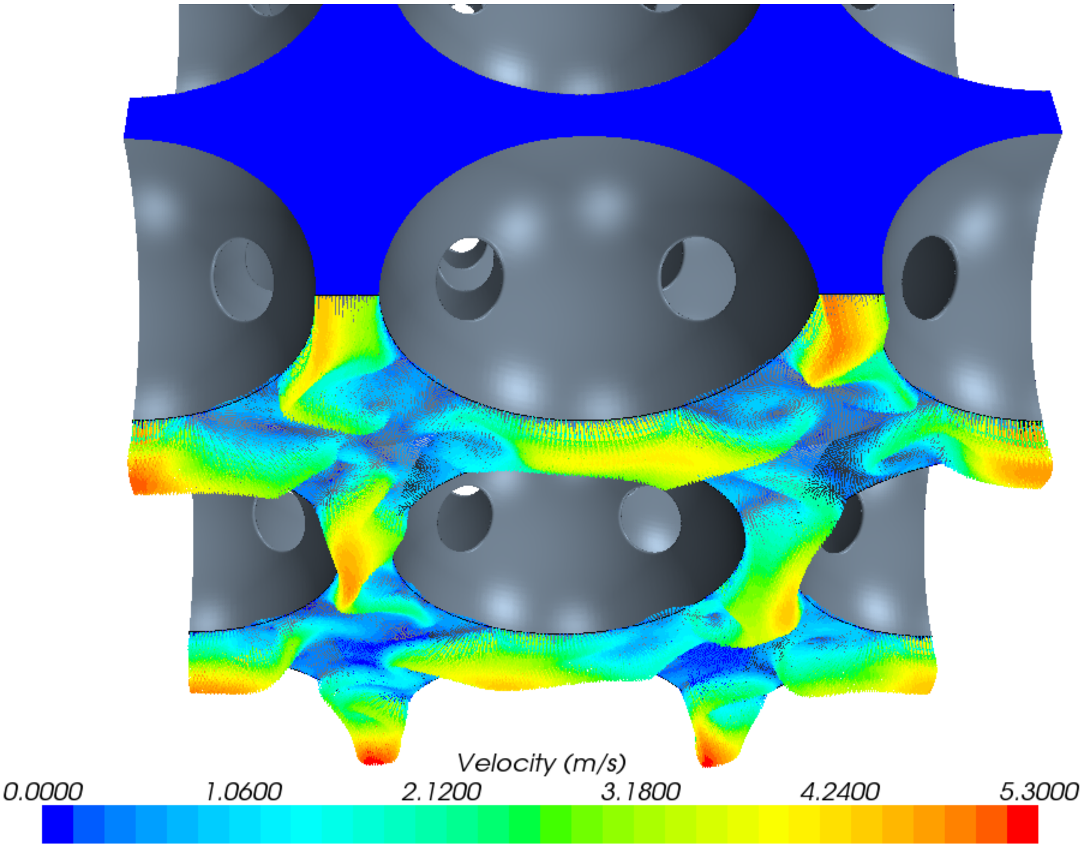

Fig. 27. Velocity vector for the realizable k-epsilon model

to assume that the pressure-strain redistribution term has a good effect on the fluid flow profile shown above as well.

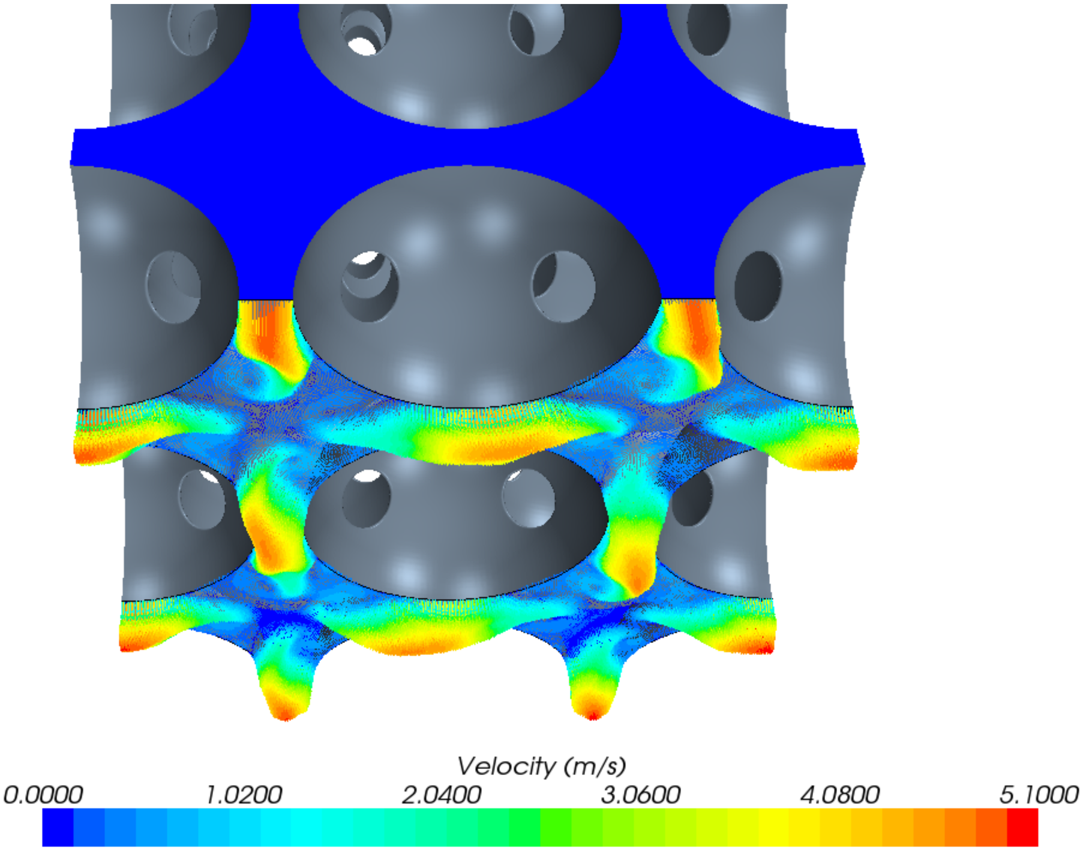

Fig. 28. Velocity vector for the Reynolds stress transport model

CHAPTER VII

CONCLUSION

Fluid flow analysis inside the PBMR core is extremely important from safety, as well as efficient designing standpoint. Two Bravais lattice structures were used in this analysis, simple cubic, and body centered cubic. Realizable k-epsilon model proved to be adequate for the simple cubic geometry. The computational pressure drop obtained for the simple cubic geometry complimented previous existing correlation well. The computed fluid flow profile for the simple cubic geometry was similar to the expected profile. Perhaps, this agreement is due to the fact that simple cubic structure is a relatively simple geometry.

On the other hand, the body centered cubic case resulted in different results from the three turbulence models that were used. The pressure drop results that were obtained form each of the turbulence models were far from the existing correlations. The standard k-epsilon model ignores most of the turbulence physics and phenomenon that should occur in a geometry like the body centered cubic. Realizable k-epsilon model is a significant improvement from the standard k-epsilon model. It uses the flow parameters to obtain certain unknowns that are just used as constants in the standard k-epsilon case. However, the realizable k-epsilon it still not good enough for a geometry like the body centered cubic. This is probably due to the high vorticity nature of the flow, where realizable k-epsilon has proved to be inadequate.

Reynolds stress transport model is perhaps the most advanced and accurate out of all the models considered in this analysis. It attempts to solve the Reynolds stress evolution equation rather than modeling it, like in the case of standard and realizable k-epsilon models. However, in the case of Reynolds stress transport model there are certain issues that need to be addressed. The linear pressure-strain model in the

Reynolds stress transport model, that was used in this analysis, has some assumptions that lead to big errors. The linear pressure strain model has three components, a rapid component, slow component and a transport component. Out of the three, the slow component is modeled using the return to isotropy hypothesis. However, the assumptions that are used in return to isotropy hypothesis are not correct in the case of body centered cubic geometry. To avoid this problem, it is suggested to use the quadratic pressure strain relation, but it is harder to reach convergence with the quadratic model.

Given the computational cost and the convergence issues associated with the Reynolds stress transport model. It is recommended to use large eddy simulation (LES) for problems with geometries like the body centered cubic. LES has an added benefit of temporal resolution over the Reynolds stress transport model with a similar computational time cost. Finally, a finer mesh is required to conduct LES or Reynolds stress transport(quadratic pressure strain) model. A finer mesh would increase the computational cost and the need for computer resources, on the other side, it will help analyze the fluid flow inside geometries like body centered cubic with lower errors and finer resolution.

REFERENCES

[1] A.G. Tomboulides, S.A. Orszag, G.E. Karniadakis, “Direct and large eddy simulations of the flow past a sphere,” *International Symposium on Engineering Turbulence Modeling and Measurements*, pp. 73–282, 1993.

[2] P. Bagchiand, S. Balachandar, “Steady planar straining flow past a rigid sphere at moderate Reynolds number,” *Journal of Fluid Mechanics*, vol. 466, pp. 365–407, 2002.

[3] V.A. Gushchin, A.V. Kostomarov, P.V. Matyushin, “Direct numerical simulation of the transitional separated fluid flows around a sphere and a circular cylinder,” *Journal of Wind Engineering and Industrial Aerodynamics*, vol. 90, pp. 341–358, 2002.

[4] E.E. Dominguez-Oniveros, C. Estrada-Perez, Y.A. Hassan, “Measurements of flow modification by particle deposition inside a packed bed using time-resolved PIV,” *HTR2008-58330*, September 28-October 01, Washington, DC, USA.

[5] M.H. Kim, H.S. Lim, W.J. Lee, “Computational fluid dynamics assessment of the local hot core temperature in a pebble-bed type very high temperature reactor,” *Journal of Engineering for Gas Turbines and Power*, vol. 131, pp. 9051–9056, 2009.

[6] S. Ion, D. Nicholls, R. Matzie, D. Matzner, “Pebble bed modular reactor the first Generation IV reactor to be constructed,” presented at the World Nuclear Association, Queen Elizabeth II Conference Centre, UK, 3-5 September 2003.

[7] Idaho National Engineering and Environmental Laboratory, 2001, Modular pebble-bed reactor project, available http://web.mit.edu/pebble-bed, 2001.

[8] U.S. DOE Nuclear Energy Research Advisory Committee and the Generation IV International Forum “A A Technology Roadmap for Generation IV Nuclear Energy Systems” *Generation IV International Forum*, December 2002.

[9] F. Safidesh, “Status of the small modular fluidized bed light water nuclear reactor concept,” *Nuclear Engineering and Design*, vol. 167, pp. 203–214, 1996.

[10] International Atomic Energy Agency, “High temperature gas cool reactor technology development,” *Proceedings of a Technical Committee meeting*, South Africa, pp. 59–71, 1996.

[11] D.L. Youchison, M.T. North, J.E. Lindemuth, J.M. McDonald and T.J. Lutz, “Thermal performance and flow instabilities in a multi-channel, helium-cooled, porous metal divertor module,” *Fusion Engineering and Design*, vol. 49, pp. 407-415, 2000.

[12] Gokhan Yesilyurt, “Numerical simulation of flow distribution for pebble bed high temperature gas cooled reactors,” Masters Thesis, Texas A&M University, College Station, Texas, May 2003.

[13] I.B. Celik, U. Ghia, P.J. Roache, C.J. Freitas, H.Coleman and P.E. Raad, “Procedure for estimation and reporting of uncertainty due to discretization in CFD applications,” *Journal of Fluids Engineering*, vol. 130, 2008.

[14] Tsan-Hsing Shih, William W. Liou, Aamir Shabbir, Zhigang Yang and Jiang Zhu , “A new k-epsilon eddy viscosity model for high Reynolds number turbulent flows,” *Computers FLuids*, vol. 24, pp. 227–238, 1995.

[15] J.L. Lumley, “Some comments on turbulence,” *Physics of Fluids*, vol. 4, pp. 203, 1992.

[16] Stephen B. Pope, *Turbulent Flows*. New York: Cambridge University Press, 1st edition, 2000.

[17] *CD-ADAPCO, StarCCM+ manual version 5.02.009*, Melville, New York, 2009.

[18] B.E. Launder, G.J. Reece, and W. Rodi, “Progress in the development of a Reynolds-stress turbulence closure,” *Journal of Fluid Mehcanics*, vol. 68, pp. 537–566, 1975.

[19] X.Cai and G. Su, “Investigation of pressure drop for fluid flow through porous media: application to a pebble-bed reactor,” in *Proceedings of 18th International Conference on Nuclear Engineering*, Xi’an, China, May 17-21, 2010.

APPENDIX A

FIGURES

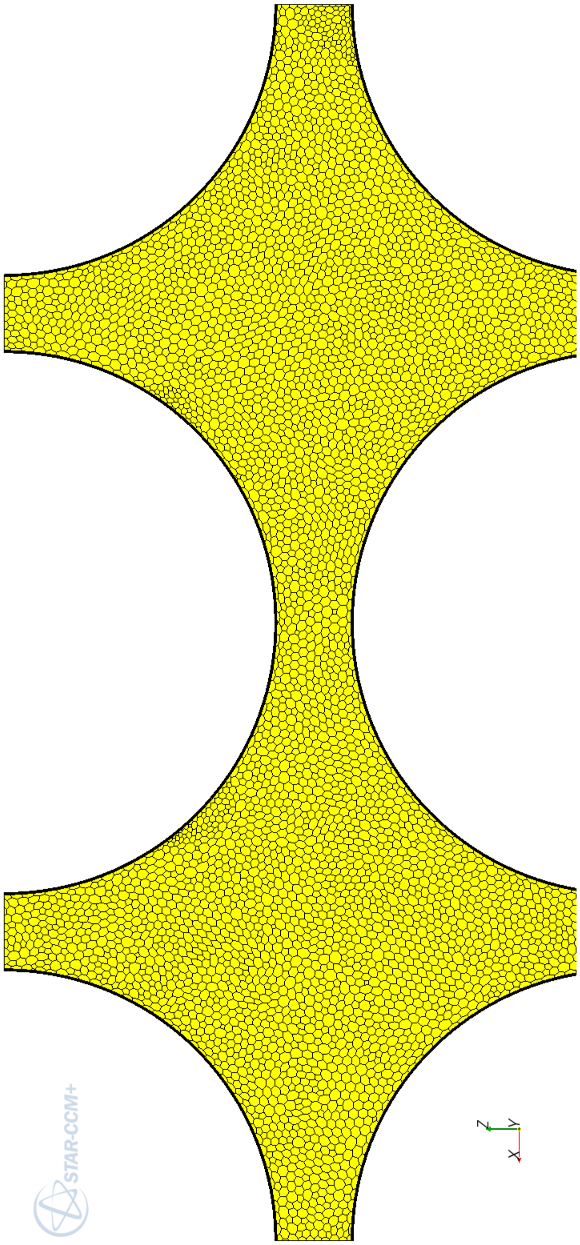

Fig. 29. Mesh 1 for body centered cubic geometry

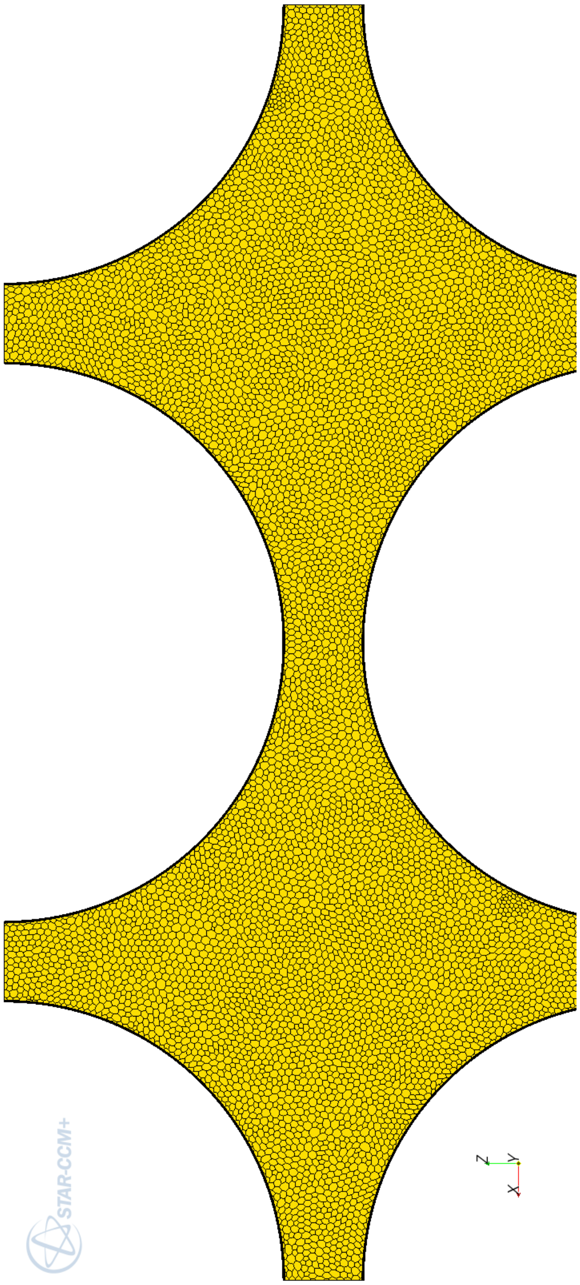

Fig. 30. Mesh 2 for body centered cubic geometry

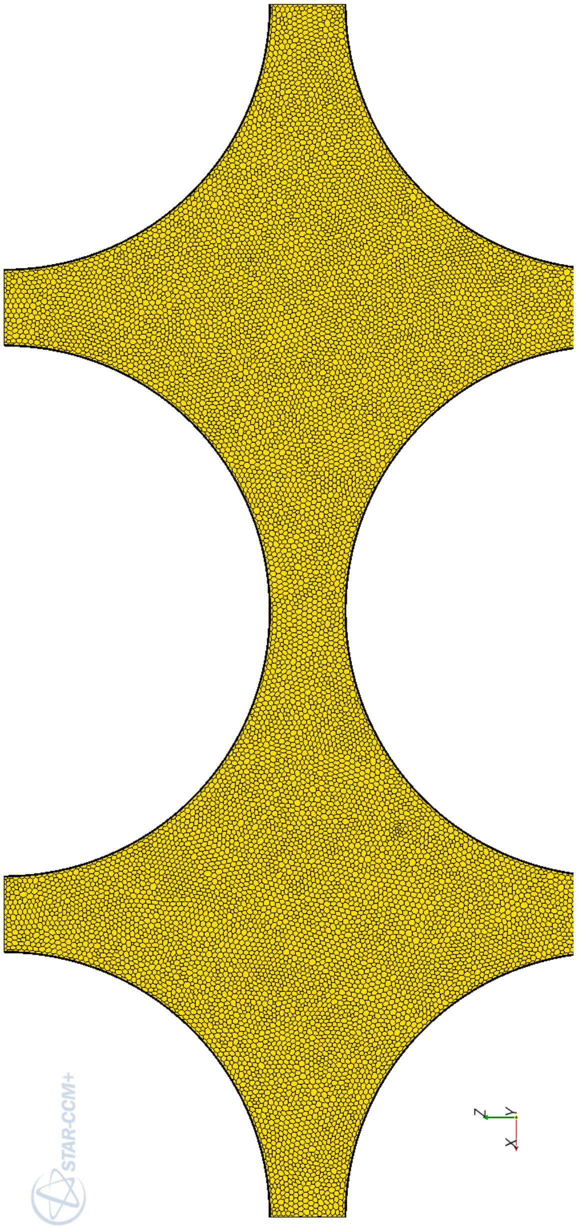

Fig. 31. Mesh 3 for body centered cubic geometry

VITA

Akshay Gandhir was born in New Delhi, India. He obtained his undergraduate degree in nuclear engineering from Texas A&M University in 2009. He enrolled in the Department of Mechanical Engineering at Texas A&M University after his undergraduate degree. He obtained his Master of Science (MS) degree in August 2011. from Texas A& University. He works in the area of fluid dynamics with a strong interest and passion for turbulence theory and modeling, computational fluid dynamics, numerical methods and other fluid flow applications. To contact Akshay Gandhir please mail the Department of Nuclear Engineering, Texas A&M University, TAMU, College Station, Texas 77843-3133.

The typist for this thesis was Akshay Gandhir.